Multiplying (39) by $2\frac{d\alpha}{dz}$ and using the equality: $\frac{d}{dz}\left(\frac{d\alpha}{dz}\right)^2 = 2\,\frac{d\alpha}{dz}\,\frac{d^2\alpha}{dz^2}$, this equation reduces to :

$$A_{\rm gas}\,\frac{d}{dz}\left(\frac{d\alpha}{dz}\right)^2 \;=\; 2\,\frac{d\alpha}{dz}\,\left\{e^{\alpha} + C_s\,(e^{\alpha})^{p_{\rm gs}} + (\rho_{\rm halo} + \rho_{\rm rot})\right\}\;.$$

Integrating the RHS with respect to α yields:

$$A_{\rm gas}\,\frac{d}{dz}\left(\frac{d\alpha}{dz}\right)^2 \;=\; 2\,\frac{d}{dz}\left\{e^{\alpha} + \frac{C_s}{p_{\rm gs}}\,(e^{\alpha})^{p_{\rm gs}} + (\rho_{\rm halo} + \rho_{\rm rot})\;\alpha + C\right\}\;.$$

For any physical system, the restoring force vanishes at the midplane (i.e. the RHS of [35] equals zero), so that $\left.\frac{d\alpha}{dz}\right|_{\rm z=0} = 0$. Thus the integration constant C is given by:

$$C \;=\; -\rho_{\rm gas}(0)\;\left\{\;\left(1 + \rho'_{\rm s,g}\;p_{\rm sg}\right)\;+\;\left(\rho'_{\rm h,g} + \rho'_{\rm r,g}\right)\;\ln\rho_{\rm gas}(0)\;\right\}\;, \tag{40}$$

where the primed variables are defined as follows:

$$\rho'_{\rm s,g} \;=\; \frac{\rho_{\rm stars}(0)}{\rho_{\rm gas}(0)}\;;\quad \rho'_{\rm h,g} = \frac{\rho_{\rm halo}(0)}{\rho_{\rm gas}(0)}\;;\quad \rho'_{\rm r,g} = \frac{\rho_{\rm rot}(0)}{\rho_{\rm gas}(0)}\;. \tag{41}$$

Thus:

$$\sqrt{\frac{-2}{A_{\rm gas}}}\;\left\{-\left(\rho_{\rm gas} + \frac{C_s}{p_{\rm gs}}\,(\rho_{\rm gas})^{p_{\rm gs}} + (\rho_{\rm halo} + \rho_{\rm rot})\;\ln\rho_{\rm gas} + C\right)\right\}^{+0.5} \;=\; \frac{d\alpha}{dz}$$

Rearranging terms and integrating yields:

$$\sqrt{\frac{A_{\rm gas}}{-2}}\;\int_{\rho_{\rm gas}(0)}^{\rho_{\rm gas}(z)}\frac{d\rho_{\rm gas}}{\rho_{\rm gas}}\;\left\{-\left(\rho_{\rm gas} + \frac{C_s}{p_{\rm gs}}\,(\rho_{\rm gas})^{p_{\rm gs}} + (\rho_{\rm halo} + \rho_{\rm rot})\;\ln\rho_{\rm gas} + C\right)\right\}^{-0.5} \;=\; z(\rho_{\rm gas}(z))\;.$$

Normalizing the gas distribution, i.e. defining $y = \frac{\rho_{\rm gas}(z)}{\rho_{\rm gas}(0)}$, inserting the integration constant C and using (36) and (38) I find:

$$z_{\rm gas}(Y) \;=\; \sqrt{\frac{\sigma^2_{\rm z,gas}}{8\pi G\;\rho_{\rm gas}(0)}}\;\;\times$$

$$\int_Y^1 \frac{dy}{y}\sqrt{\left(\frac{1}{(1+\rho'_{\rm s,g}\;p_{\rm sg}) - (y + \rho'_{\rm sg}\;p_{\rm sg}\;y^{p_{\rm gs}}) - (\rho'_{\rm h,g} + \rho'_{\rm r,g})\ln(y)}\right)}\;. \tag{42}$$

Notice that the term ($\rho'_{\rm s,g}\, p_{\rm sg}$) equals the ratio of stellar and gaseous kinetic energy in the midplane. For vanishing stellar, halo, and rotational densities (i.e. $\rho'_{\rm s,g} = \rho'_{\rm h,g} = \rho'_{\rm r,g} = 0.0$ so that the gas is fully self-gravitating), it can be shown that (42) then reduces to the familiar self-gravitating solution, $\rho_{\rm gas}(z) \propto {\rm sech}^2(z/z_0)$, indeed.

Investigating Eqn. (42), we see that there is no solution possible when the sum of the rotation and DM-halo density is negative (i.e. for a steeply rising rotation curve) because at small fractional densities, Y, the logarithmic term goes to $-\infty$ and hence dominates, leading to a negative term inside the square root. Bottema *et al.* (1987), applying the local approach, find that the rotation term can contribute significantly in the steeply rising parts of galactic rotation curves. Obviously, since galaxies do not have holes in those regions where the rotation curve rises, at least one of the assumptions must break down. Most likely, deviations from cylindrical symmetry become important and the equation of hydrostatic equilibrium is no longer a good approximation to the vertical Jeans equation.

An iterative procedure is followed to find the vertical density distribution of the gas. Starting from initial guesses for stars and gas, a solution of (42) is calculated, which provides a new (normalized) z-distributions for the first component. Note that this equation can be inverted to calculate the vertical distribution of the stars from the z-distribution of the gas merely by interchanging the g and s indices. In order to eliminate numerical instabilities, I chose the calculated component (i.e. the LHS of [42]) to be the component with the smallest velocity dispersion. The normalized distribution, $z_{\rm gas}(Y)$ is then inverted to yield $\rho_{\rm gas}(z)$ which is then scaled so that its z-integral yields the appropriate surface density. The stellar density distribution is then calculated by raising the gaseous distribution to the power $p_{\rm gs}$ (i.e. applying the equivalent of Eqn. [36]) followed by the surface density normalization. From the new midplane values the next solution of (42) is calculated, ... until consecutive changes become small. For a given stellar velocity dispersion, the stellar vertical density distribution changes in each iteration step. In order to keep the thickness of the stellar disk fixed, as suggested by observation (vdKS81a&b; vdKS82a&b; BD93), I change the stellar velocity dispersion after each iteration step accordingly. This procedure can be easily expanded to include “N” isothermal components.

The local dark matter density can be determined in an iterative manner as well. An upper limit to the local dark matter density can be found by assuming that all other components are massless. Using the Gaussian-equivalent method [Eqn. (14)], the measured width and velocity dispersion of the gas layer the upper limit of the dark matter density is calculated. A lower limit to the local dark matter density is of course zero. For a values of the dark matter density halfway between the lower and upper limit, the model gas-layer thickness is calculated and compared with the observed value. If the calculated thickness corresponding to this trial DM-density value is larger than the observed value, then the lower bound is increased to the trial value. This procedure is repeated until convergence is reached. Model calculations show that beyond the optical disk, it is possible to accurately recover the input [into Eqn. (42)] DM densities from simulated thickness measurements.

2.8. APPENDIX-D: FOUR SPECIAL CASES

Here I describe the gaseous distribution in the vertical direction for four interesting limiting cases with very different flaring behavior. In the first three of those, the rotation curve is assumed to be constant, while the fourth case represents gas in a region where the rotation curve is falling. In all but the self-gravitating case, the gas is treated as a massless testparticle component. The results are listed below, where all widths, W_{gas} [$\approx FWHM/2.35$, as defined by Eq. (5)], are expressed in kpc.

Fully self – gravitating gas :

$$W_{\rm gas}^{\rm self}(R) \;\approx\; 6.74\left(\frac{\sigma_{10}^2}{\Sigma_1(R)}\right) \tag{43}$$

Gas in a stellar disk :

$$W_{\rm gas}^{\rm stars}(R) \;\approx\; 0.113\sqrt{\left(\frac{z_{0,400}}{\mu_{100}(0)\ \mathcal{M}/\mathcal{L}}\right)} \times \sigma_{10} \quad \exp\frac{R}{2h_{\rm R}} \tag{44}$$

Gas in a (flattened) dark halo mass distribution :

$$W_{\rm gas}^{\rm halo}(R) \;\approx\; \sqrt{q\left(\frac{2.436}{1.436\ +\ q}\right)} \times \left(\frac{\sigma_{10}}{V(\infty;1)_{\rm halo,100}}\right)\sqrt{R_{\rm c,10}^2 + (R_{10}/\mathcal{C}(q))^2} \tag{45}$$

Gas in Keplerian falloff region :

$$W_{\rm gas}^{\rm rot}(R) \;=\; 0.484\,\frac{\sigma_{10}}{\sqrt{M_{\rm tot,11}}}\,R_{10}^{\frac{3}{2}} \tag{46}$$

where σ_{10} is the gaseous velocity dispersion in units of 10 km s^{-1}, $\Sigma_1(R)$ the gaseous surface density in units of solar masses per pc^2, $z_{0,400}$ the scale height of the stars in units of 400 pc, $\mu_{100}(0)$ the central surface brightness in units of 100 $L_\odot$/pc^2, $\mathcal{M}/\mathcal{L}$ is the number of solar masses per solar luminosity, $h_{\rm R}$ is the radial scale length of the (exponential) stellar disk, $V(\infty;1)_{\rm halo,100}$ the asymptotic rotation velocity of the round dark halo in units of 100 km s^{-1}, $R_{\rm c,10}$ the core radius of the dark halo in units of 10 kpc, R_{10}, the galactocentric radius in 10 kpc, $\mathcal{C}(q)$, is the core radius correction factor arising from the flatness,q, of the DM halo [is of order unity, see Eqn. (22)], and $M_{\rm tot,11}$ the total mass of the galaxy in units of 10^{11} $M_\odot$.

Notice that the thickness of the gas layer in a potential which is completely dominated by the rotation density is of the same order of magnitude as a gas layer in a DM-halo potential only. Such situations may arise for galaxies where the rotation curve falls in a close to Keplerian manner.

If one really wants to use the local approach (e.g. for quick estimation purposes) instead of the global approach, one might as well use the approximation to Eqn. (42) I found to be accurate to about 10% over a wide range of parameters. $W_{\rm gas}^{\rm approx}$ can be found from:

$$\left(\frac{1}{W_{\rm gas}^{\rm approx}}\right)^2 = \left(\frac{w_{\rm g}}{W_{\rm gas}^{\rm self}}\right)^2 + \left(\frac{1}{W_{\rm gas}^{\rm no-self}}\right)^2 , \tag{47}$$

where

$$\left(\frac{1}{W_{\rm gas}^{\rm no-self}}\right)^2 = \left(\frac{1}{W_{\rm gas}^{\rm stars}}\right)^2 + \left(\frac{w_{\rm hr}}{W_{\rm gas}^{\rm halo}}\right)^2 + \left(\frac{w_{\rm hr}}{W_{\rm gas}^{\rm rot}}\right)^2 , \tag{48}$$

with

$$w_{\rm g} = \frac{(1.15\ \Sigma_{\rm gas} + 1.55\ (\Sigma_{\rm stars} + \Sigma_{\rm halo} + \Sigma_{\rm rot}))}{(\Sigma_{\rm gas} + \Sigma_{\rm stars} + \Sigma_{\rm halo} + \Sigma_{\rm rot})} ,$$

$$w_{\rm hr} = \frac{(1.20\ \Sigma_{\rm stars} + 1.05\ (\Sigma_{\rm halo} + \Sigma_{\rm rot}))}{(\Sigma_{\rm stars} + \Sigma_{\rm halo} + \Sigma_{\rm rot})} ,$$

and

$$\Sigma_{\rm halo} = \rho_{\rm halo} \times W_{\rm gas}^{\rm no-self} \quad \text{and} \quad \Sigma_{\rm rot} = \rho_{\rm rot} \times W_{\rm gas}^{\rm no-self} ,$$

where the relations for the halo and rotation surface densities are evaluated [Eqn. (48)] using $w_{\rm hr} = 1.0$. The widths, $W_{\rm gas}^{\rm i}$, are the widths as found for the special cases [according to Eqns. (43), (44), (45) and (46)]. Inside the stellar disk, the width of the gas layer is mostly determined by the gas-inside-stellar-disk term, $W_{\rm gas}^{\rm stars}$. Beyond, the halo-term, $W_{\rm gas}^{\rm halo}$, dominates. The self-gravity of the gas perturbs the dominant term slightly, but with a different numerical coefficient for the two regimes because of the different form of the un-perturbed z-distribution functions ($\mathrm{sech}^{2p_{\rm sg}}(z/z_0)$ versus Gaussian respectively).

I have tested this approximation for several cases. The first case corresponds to BE89's mass distribution for NGC 3198. The second case corresponds to a γ=0.6-disk in a flattened ($q = 0.1$) dark halo, thereby minimizing the stellar and maximizing the dark halo contribution. The third case consists of BE89's halo and stellar mass model but with the gas surface density multiplied by a factor of ten. In the last test case I also multiply the halo densities by a factor of ten. In all these cases Eqn. (47) recovers the exact solution to Eqn. (42) to within 10 %.

REFERENCES

Albada, T.S., van, Bahcall, J.N., Begeman, K., Sancisi, R., 1985, ApJ, 295, 305 (ABBS85)

Albada, T.S. van, Sancisi, R., 1986, Phil. Trans. R. Soc. Lond. A., 320 447

Athanassoula, E, Bosma A., Papaioannou, P., 1987,A&A, 179, 23 (ABP87)

Bahcall, J.N., 1984 , ApJ, 276, 156

Bahcall, J.N., Casertano, S., 1985, ApJ, 293, L7

Barteldrees, A., Dettmar, R.J., 1994, A&AS, 1994, 103, 475

Begeman, K.G., 1987, Ph. D. Thesis, Rijksuniversiteit te Groningen

Begeman, K.G., 1989, A&A, 223, 47 (BE89)

Blitz, L., Magnani, K., Mundy, L., 1984, ApJ, 282, L9

Bosma, A., 1978, Ph.D. Thesis, University of Groningen

Bottema, R, 1993, A&A, 275, 16

Bottema, R, van der Kruit, P.C., Freeman, K.C., 1987, A&A, 178, 77

Broeils, A.H., 1992, Ph. D. Thesis, University of Groningen

Carignan, C., Freeman, K.C., 1988, ApJ, 323, L33

Casertano, S., 1983, MNRAS, 203, 735

Casertano, S., van Gorkom, J.H., 1991, AJ, 101, 1231

Corradi,R.L., Boulesteix,J., Bosma,A., Amram,P., Capaccioli,L., 1991, A&A244, 27

Dekel, A, Shlosman, I, 1983, in "Internal Kinematics and Dynamics of Galaxies", IAU Symposium 100, ed. E. Athanassoula (Dordrecht, Reidel,197)

Dickey, J.M., Hanson, M.M, Helou, G., 1990, ApJ, 352, 522

Efstathiou, G, Lake, G., Negroponte, J, 1982, MNRAS, 199, 1069

Gilmore, G., Reid, N., 1983, MNRAS, 202, 1022

Hoffner, P., Sparke, L., 1994, ApJ, 428, 466

Van der Hulst, J.M., Terlouw, J.P., Begeman, K.G., Zwitser, W. and Roelfsema, P.R., 1992, in "Astronomical Data Analysis Software and Systems I", ed. D.M. Worall, C. Biemesderfer and J. Barnes, PASP Conf Series No. 25, p. 131

Kamphuis, J., 1993, Chapter 12, Ph.D. Thesis Rijksuniversiteit te Groningen

Kent, S, 1987, AJ, 93, 816

Kruit, P.C. van der, 1981, A&A, 99, 298

Kruit, P.C. van der, 1986, A&A, 157, 230

Kruit, P.C. van der, 1988, A&A, 192, 117

Kruit, P.C. van der, Searle, L., 1981a, A&A, 95,105 (vdKS81a)

Kruit, P.C. van der, Searle, L., 1981b, A&A, 95,116 (vdKS81b)

Kruit, P.C. van der, Searle, L., 1982a, A&A, 110, 61 (vdKS82a)

Kruit, P.C. van der, Searle, L., 1982b, A&A, 110, 79 (vdKS82b)

Kruit, P.C. van der, Shostak, G.S., 1982, A&A, 105, 351

Knapp, G.R., 1987, PASP, 99, 1134

Kuijken, K., Gilmore, G., 1989, MNRAS, 239, 571 (KG89)

Kundić T., Hernquist, H., Gunn, J.E., 1993, p 592 in "Back to the Galaxy", AIP Conference proceedings # 278, Editors S.S. Holt, F. Verter

Lake, G., Feinswog, L., 1989, AJ, 98, 166 (LF89)

Malhotra, S., 1994, ApJ, 433, 687

Maloney, P., 1992, p. 117, in "The Evolution of Galaxies and their Environment", 1992, NASA conference Publication 3190, Editors D. Hollenbach, H. Thronson, J.M. Shull

Maloney, P., 1993, ApJ, 414, 41 (M93)

Merrifield, M.R., 1992, AJ, 103, 1552

Olling, R., Gorkom, J.H. van, 1992, p. 374 in "The Evolution of Galaxies and their Environment", 1992, NASA conference Publication 3190, Editors D. Hollenbach, H. Thronson, J.M. Shull

Olling, R., Gorkom, J.H. van, 1995, in "Dark Matter", 5^{th} Astrophysics Conference in Maryland, AIP Conference proceedings (in press)

Persic, M., Salucci, P., 1988, MNRAS,243, 131

Pfenniger, D., Combes, F., Martinet, L., 1994a, A&A, 285, 79

Pfenniger, D., Combes, F., 1994b, A&A, 285, 94

Press, W.H., Flannery, B.P, Teukolsky, S.A., Vetterling, W.T., 1990, in "Numerical Recipes", Cambridge University Press

Pritchet, C., 1983, AJ, 88, 1476

Rubin,V.C., Ford, W.K., Thonnard, N., 1980, ApJ, 238, 471

Rupen, M.P., 1991, Ph.D. thesis, Princeton University

Sackett, P.D, Sparke, L.S., 1990, ApJ, 361, 408 (SS90)

Sackett, P.D., Rix, H.W., Jarvis, B.J., Freeman, K,C., 1994, ApJ, 436, 629 (SRJF94)

Sackett, P.D., Morrison, H.L., Harding, P., Boroson, T.A., 1994b , Nature, 370, 11 August p. 441

Sancisi, R., Allen, R.J., 1979, A&A, 74, 73

Sparke, L, Casertano, S, 1988, MNRAS, 234, 873

Shostak, G.S., Kruit, P.C. van der, 1984, A&A, 132, 20

Toomre, A, 1983, in "Internal Kinematics and Dynamics of Galaxies" , IAU Symposium 100, ed. E. Athanassoula (Dordrecht, Reidel,177)

Wainscoat, R.J., Freeman, K.C., Hyland, A.R., 1989, ApJ, 337, 163

Yoshi, Y.,Ishida, K., Stobie, R.S, 1987, AJ, 93, 232

Chapter 3

Paper II, to be submitted to AJ

3. The Highly Flattened Dark Matter Halo of NGC 4244

ABSTRACT

In a previous paper (Olling 1995, AJ, 110, 591;Chapter 2) a method was developed to determine the shapes of dark matter halos of spiral galaxies from an accurate determination of the rotation curve and the flaring of the gas layer. Here this method is applied to the almost edge-on spiral NGC 4244.

I present sensitive high resolution VLA B, C, and D array observations in the 21-cm spectral line of neutral atomic hydrogen of the nearby Scd galaxy NGC 4244. The gas layer of NGC 4244 is rather symmetric in all respects, e.g. the surface density distribution, flaring and warping. This allows for a reliable determination of the rotation curve, despite the fact that it is close to edge-on. The rotation curve rises slowly in the inner 6 kpc, is roughly constant at 100 km s^{-1} until 10 kpc, and decreases in Keplerian fashion by 15% at the last measured point at 14 kpc. The rotation curve constrains the stellar mass-to-light to lie between 50 and 100% of the "maximum-disk" $M/\mathcal{L}$ value.

The observed flaring of the H I beyond the optical disk puts significant constraints on the dark matter halo, which are almost independent of the stellar mass-to-light ratio. I find that NGC 4244's dark matter halo is highly flattened: $q_\rho = c/a = 0.2^{+0.3}_{-0.1}$. Alternatively, the measured flaring curve is consistent with a round halo if the gaseous velocity dispersion ellipsoid is anisotropic. In that case the vertical dispersion of the gas is 50 - 70% of the measured tangential velocity dispersion.

A new technique is presented to determine simultaneously the inclination and the thickness of the gas layer from high resolution H I observations. This procedure uses the apparent widths at many azimuths rather than just the edge channels, and can be used at inclinations as low as 60^o .

3.1. INTRODUCTION

Although rotation curves of spiral galaxies have been used as evidence for the presence of dark matter (DM), little is known about the nature, extent and actual distribution of the DM halos (e.g., van Albada *et al.* 1985; Lake & Feinswog 1989). As measurements of the equatorial rotation curve probe the potential in only one direction, they provide no information about the shape of the DM halos.

In a previous paper, Paper I (Olling 1995; Chapter 2), it was shown that measurements of the radial variation of the thickness of gas layers (flaring) can be used to constrain the shape of the DM halo. This is accomplished by comparing the measured flaring with that expected from a self-gravitating gaseous disk, with the observed velocity dispersion, in an axisymmetric potential generated by the stellar disk and (flattened) DM halo. The method of calculation which produces the most reliable model flaring curve is the *global* approach, in which the potential is calculated from the *total* mass distribution of the galaxy (Paper I). In this paper the method is applied to the galaxy NGC 4244.

In the past, several methods have been used to determine the shape of the dark matter halos. Hoffner & Sparke (1994) analyzed the warping behavior of H I disks and concluded that only one (NGC 2903) of the five systems studied requires a DM halo as flattened as E4[13]. On the other hand, in studies of polar ring galaxies (Sackett & Sparke 1990; Sackett *et al.* 1994; Sackett & Pogge 1995) substantially flattened DM halos are found (E6-E7 for NGC 4650A, E5 for A0136-0801). The shape of the dark halo of the Milky Way has been estimated (E0 - E7) from the kinematics of extreme Population II stars (Binney & Ostriker 1987b; Sommer-Larsen & Zhen 1990; van der Marel 1991; Amendt & Cuddeford 1994). Steiman-Cameron *et al.* (1992) used the dynamics of the precessing dusty disk of the S0 galaxy NGC 4753 to infer the shape of the DM halo (E1).

Van der Kruit (1981) used measurements of the thickness of NGC 891's gas layer to infer the midplane matter density within the optical disk. He found that the scale length of the total matter (luminous plus dark) was similar to the scale length of the light distribution and concluded that the mass-to-light ratio does not vary significantly with radius. Since mass models where all the mass is concentrated in the disk require large radial changes in the $M/\mathcal{L}$ to reproduce the observed flat rotation curves, the DM halo is not as highly flattened as the stellar disk. A similar conclusion was reached for NGC 4565 (Rupen 1991a) and the Milky Way (Knapp 1987; Merrifield 1992; Malhotra 1994). As we can measure the light distribution of the stellar disk only and have no prior knowledge of the mass-to-light ratio of stellar disks, the relative contribution of luminous and dark matter to a given rotation curve are not known. Models of galaxy formation which include simple estimates of the star formation history (e.g., Larson & Tinsley 1978) predict $M/\mathcal{L}$'s which are in the range of values derived from observed rotation curves (e.g., Rubin *et al.* 1985; Athanassoula *et al.* 1987; Bottema 1988; Broeils 1992, Chap. 12). However, different star formation histories can easily result in mass-to-light ratios which differ by a factor of a few (e.g., Tinsley 1981; Worthey 1994; de Jong 1995, Chap. 4). An upper limit to the mass-to-light ratio, and hence a lower limit to the amount of DM, can be obtained by assuming that the peak of the observed rotation curve is due to the stellar disk only, the so called maximum-disk hypothesis (van Albada & Sancisi 1986). Employing the maximum-disk model, Broeils (1992) finds that the ratio of dark to luminous matter lies between 0.5 and 10, where the larger values are found for the low mass systems. Other $M/\mathcal{L}$ estimators have been used (van der Kruit 1981; Efstathiou *et al.* 1982; Athanassoula *et al.* 1987; Martinet 1988; Bottema 1993), typically yielding a stellar disk 50% - 100% as massive as the "maximum-disk". The allowed range in dark-to-luminous matter ratio might thus be twice larger than determined by Broeils. But

[13] A spheroidal system with shortest-to-longest axis ratio c/a (q_ρ) of the density contours has a shape En, with n such that $q_\rho = 1 - n/10$

note that the total mass of the system is hardly affected by this trade off between luminous and dark matter.

In a study similar to the present one, Rupen (1991a) analyzed high resolution H I observations of two edge-on galaxies, NGC 4565 and NGC 891. For these galaxies he finds that the flaring data imply stellar disks with masses two-third and one-half as massive as "maximum-disk", consistent with van der Kruit's (1981, 1988) results for NGC 891. In addition, Rupen found that non-thermal pressure is probably not an important contributor to the total pressure. The fact that NGC 891 and NGC 4565 have similar gas layer widths and similar luminous mass distribution but very different magnetic energy densities argues against a significant magnetic pressure contribution. Due to the increased sensitivity of the VLA, sensitive high resolution H I observations, as pioneered by Rupen (1991b), can now be routinely obtained and processed. The high resolution H I data presented in this paper are sensitive enough to determine the gaseous velocity dispersion and probe the region beyond the optical disk where the thickness of the gas layer is most sensitive to the shape of the DM halo. The new method to determine the thickness of the gas layer (presented in Sec. 3.5.) complements an existing method specific to the case of strong spiral structure in H I (Braun 1991), and is more general than the method employed by Irwin & Seaquist (1991).

NGC 4244 is an intermediate mass system with a rotation speed of about 100 km/s. Its proximity (3.6 Mpc) results in the high linear spatial resolution (17.5 pc/arcsec) which is necessary to successfully determine both the vertical structure of the gaseous disk and the rotation curve in the inner parts of the galaxy. The large inclination of NGC 4244 with respect to the line of sight, about $84\overset{\circ}{.}5$ degrees, allows for an accurate determination of the rotation curve. NGC 4244 is one of the few galaxies to show, on both sides, the characteristic drop in rotation velocity beyond the optical disk.

The outline of this paper is as follows: in Sec. 3.2. I summarize current observational knowledge of NGC 4244. The new H I observations and the parameters derived therefrom are presented in Sec. 3.3.. A new method to derive the thickness and inclination of the gas layer is outlined in Sec. 3.5.1.. This method is applied in Sec. 3.5.2.. In Sec. 3.6. I describe how, in conjunction with self-consistent mass models, the observed flaring can be used to constrain the shape of the dark matter halo. The shape of the halo is then determined in Sec. 3.6.1.. Some caveats related to various step along the way are discussed in Sec. 3.8.. The implications of the highly flattened halo for the amount and nature of dark matter are discussed in Sec. 3.9..

3.2. THE GALAXY NGC 4244

NGC 4244 is a small almost edge-on ScdIII galaxy in which individual stars and H II regions can be resolved (Sandage & Bedke 1994). Surface brightness photometry (van der Kruit & Searle 1981a) reveals that the radial light distribution is close to exponential till about five optical scale lengths, where it cuts off sharply (see also Fig. 16). The vertical scale height of the light is constant with radius, while no thick disk is present. The very faint bulge ($\mu_K(r_e) = 23.05$) with an effective radius of 140$''$ (Bergstrom *et al.* 1992) is dynamically insignificant.

There are several indications that the current star formation rate is very low in NGC 4244. Only very low radio continuum emission (Condon 1987) and little Hα emission (Walterbos 1994, private communications) has been detected, while upper limits have been set on X-ray emission (Bregman & Glassgold 1982) and emission from highly ionized halo gas (Deharveng *et al.* 1986). Very faint radio continuum emission extends along the plane of the galaxy from 2$'$.5 north-east (NE) to 2$'$ south-west (SW) of the center. The 60μm emission is enhanced in this region as well (Rice 1993). In contrast to most galaxies (Bicay & Helou 1990), NGC 4244's 20 cm radio continuum emission is not more extended than the 60μm emission. The weak CO emission (Sage 1993), coincident with the radio continuum emission, amounts to 2.2 x 10^7 $M_\odot$ of H_2 (50% of the H I mass in this region). The H_2 radial surface density distribution is calculated with the Abel inversion technique (Sec. 3.4.1.) and is consistent with a Gaussian ring centered at 1.3 kpc, with a FWHM of 1.6 kpc and an amplitude of 1.6 $M_\odot$ pc^{-2}.

Throughout this paper the distance to NGC 4244 is taken to be 3.6 Mpc, consistent with the IR-Tully-Fisher distance (3.7 Mpc, Aaronson *et al.* 1986) and the "hydrogen counterpart" of the Tully-Fisher distance (3.6 Mpc) as defined by Broeils (1992, Chapter 3). NGC 4244 is the second brightest member of a group of dwarf galaxies: the CVn I (de Vaucouleurs 1975) or B4 (Kraan-Korteweg & Tammann 1979) group which contains 21 members. This group has a radius of 1 Mpc, a density of 4.5 Mpc^{-3}, and a total luminosity of 8.9 10^9 $L_{\odot,B}$. The nearest catalogued neighbor is the SmIV galaxy NGC 4190 at a projected distance of 81 kpc. This group is rather elongated (axial ratio $\sim$ 3), with the position angle of the long axis at -18^o , 66^o from the plane of NGC 4244. The observation presented in this paper (Sec. 3.3.1.) fail to detect gas rich companions more massive than 10^7 $M_\odot$ within 45 kpc.

Fig. 15 shows the optical (grey scale) image from IIIaJ photographic observations (van der Kruit & Searle 1981a) and a total hydrogen map. The orientation of the dustlane suggests that the eastern side of the galaxy is the far side and thus least affected by absorption. The intrinsic radial surface brightness distribution, $L(R)$, is derived by applying the Abel-inversion technique (Sec. 3.4.1.) to four different strips parallel to the major axis, after removal of foreground stars. The first strip contains all light perpendicular to the minor axis (top profile in Fig. 16). The second strip contains all light within 420 pc (twice the vertical exponential scale height, z_e) from the midplane. The third and forth strips are determined from those parts which are further than 420 pc from the midplane (east and west respectively). As noticed by van der Kruit & Searle (1981a), the stellar disk is truncated at somewhat different radial distances on the two sides of the galaxy. All four profiles are consistent with the same radial scale length (h_R) of 2.0 kpc, slightly larger than the value derived by van der Kruit & Searle (1981a)[14]. Thus, the overall light distribution is probably not much affected by extinction (the adopted fit is indicated by the filled circles). The IIIaJ-magnitudes are converted to B-magnitudes assuming a (B-V)=0.7 as appropriate for the old disk (Bottema 1989). Some parameters of this galaxy are listed in Table 3.

Table 3: Optical parameters

Distance	3.6 Mpc
$h_{\rm R}$	2.0 kpc
$z_{\rm e}(=\frac{1}{2}z_0)$	0.21 kpc
$R_{\rm max,SW}$	10.0 kpc
$R_{\rm max,NE}$	8.0 kpc
$\mu_{0,\rm B}$	22.4 $\pm$ 0.07 mag/$\Box''$
$\rm L_B(0)$	74.6 $\pm$ 5 $\rm L_\odot/pc^2$
D^i_{25}	11 kpc
$\rm L_{tot}(B)$	1.8 10^9 $\rm L_\odot$, $M_{\rm B}$ = -17.7

Note: No correction for galactic extinction was required ($E(B-V)$=0; Burstein & Heiles 1984). D^i_{25} is taken from de Vaucouleurs *et al.* (1976; RC2). The face-on central surface brightness is calculated *assuming* a sech^2 vertical light distribution. For a distribution which is exponential in the vertical direction L(0) is twice larger. The absolute magnitude, the central surface brightness, and the total luminosity, which are derived from the central surface brightness and $h_{\rm R}$, change accordingly (to 21.6 mag/$\Box''$, 149 $\rm L_\odot/pc^2$ and $M_{\rm B}$ = -18.4, respectively). Note that D^i_{25}-values derived from the sech^2 and exponential luminosity density distributions (9.6 and 12.6 kpc) bracket the statistically corrected RC2 value.

3.3. H I OBSERVATIONS

NGC 4244 was observed with the VLA[15] (Napier *et al.* 1983), in the 10 km (B), 3 km (C), and 1 km (D) arrays for a total of about 14 hours. The data from 1989 and 1990 were taken as part of a project aimed at doing a multi wavelength high resolution study of the interstellar medium in nearby galaxies (Braun 1995). The observing parameters are summarized in Table 4.

Standard calibration procedures were followed. After removal of some data affected by interference[16] the data were combined in the UV plane. The primary flux calibrator was 3C 286, with an assumed flux at 1418 MHz of 14.86 Jy. A heavily tapered continuum image was made using 5 line free channels on both sides of the band. The rms noise in this image is 0.94 mJy/beam at a resolution of 80$''$ x 77$''$. Several background sources but no extended radio continuum emission was detected from NGC 4244 itself down to a 3 sigma limit of 2.8 mJy/beam, consistent with a peak flux of 1.4 mJy as determined by Condon (1987) and Hummel *et al.* 's (1984) non-detection at 610 MHz. A strong background source about 7$'$ NE

[14]All the linear distances derived by van der Kruit & Searle (1981a), who use a distance of 5 Mpc (Sandage & Tammann, 1975), are scaled to the adopted distance for NGC 4244, 3.6 Mpc.

[15]The VLA of the National Radio Astronomy Observatory is a facility of the National Science Foundation operated under cooperative agreement by Associated Universities, Inc.

[16]In particular the 1992 D-array daytime observations required extensive UV-editing due to solar interference.

of NGC 4244 is probably the reason for the much stronger detection reported by Schlickeiser *et al.* (1984).

Table 4: Instrumental parameters for the VLA observations of NGC 4244

Observing dates	2 May 1989, B-array, 6 hours on source
	30 Nov 1989, D-array, 15 min on source
	29 Nov 1990, C-array, 45 min on source
	21 Aug 1992, D-array, 7 hours on source
Pointing center	$12^h\ 14^m\ 59\overset{s}{.}9$
	$38^o\ \ 5'\ \ 6''\!.0$
Velocity of band center	245 km s^{-1}, heliocentric, optical definition
Number of channels	63
channel separation	5.2 km s^{-1}
Velocity resolution	6.2 km s^{-1}
map making characteristics	beam sizes: along and $\perp$ to the major axis
$10''\!.0$ x $10''\!.0$	B + C + D-array, uniformly weighted, tapered
$28''\!.3$ x $10''\!.1$	B + C + D-array, uniformly weighted, tapered
$38''\!.0$ x $38''\!.0$	B + C + D-array, naturally weighted
$55''\!.0$ x $55''\!.0$	1992 D-array, naturally weighted
rms noise in channel maps	
$10''\!.0$ x $10''\!.0$	2.3 mJy/beam $\rightarrow$ 131 10^{18} cm^{-2}
$28''\!.3$ x $10''\!.1$	1.9 mJy/beam $\rightarrow$ 39 10^{18} cm^{-2}
$38''\!.0$ x $38''\!.0$	0.73 mJy/beam $\rightarrow$ 2.8 10^{18} cm^{-2}
$55''\!.0$ x $55''\!.0$	0.76 mJy/beam $\rightarrow$ 1.4 10^{18} cm^{-2}

For the two high resolution data sets the sensitivities listed in Table 4 correspond to roughly 3 10^4 $M_\odot$/beam/channel at the field center, while the two low resolution sets are about three times more sensitive as a result of the interim upgrade of the VLA receivers. To bring out emission at different scales images of the line emission were made with different tapering.

3.3.1. Results

Assuming low optical depth the total amount of neutral hydrogen is arrived at by adding the flux containing areas in the channel maps. The validity of this assumption is checked in Appendix 3.13.. The flux containing areas are required to have a flux larger than $\sim 1.2\sigma$ in a smoothed version of the spectral line cube (smoothed to a four and three times lower resolution, spatially and in velocity respectively). The high and low resolution total H I distributions are presented in Fig. 17. The images have been rotated 48° clockwise, so that the upper part is the north-eastern side. Both the high and low resolution data show a warp starting at the edge of the optical disk (about 9 arcmin from the center). The H I distribution of NGC 4244 is rather symmetric apart from the "popped blister" located just "below" the major axis about four arcmin to the north-east. A recent star formation event might be responsible for this feature as it coincides with peaks in the radio continuum and IRAS emission.

The low resolution, primary beam corrected, total intensity image yields a total H I mass of 1.29 ± 0.05 10^9 $M_\odot$. The north-eastern part contains 51% of the total H I mass, the south-western part amounts to 49%. The hydrogen mass determined from the global profile (the flux as a function of velocity, Fig. 18), 1.4 ± 0.1 10^9 $M_\odot$, is consistent with the determination from the total H I map. The H I mass listed in Table 5 is the average of the total H I and global profile values, with the error half the difference.

From the global profile a systemic velocity (the mean of the 10%, 20% and 50% points) of 244.4 ± 0.3 km s^{-1} is determined, in agreement with the value determined by Huchtmeier & Seiradakis (1985). As a result of the asymmetry in the H I distribution, the receding part has a higher peak value than the approaching part. The position at the major axis where the recession velocity equals the systemic velocity is offset by $7''.4 \pm 0''.6$ towards the south-west, which agrees well with the central position of the H I as determined in Sec. 3.4.1..

Within 45 kpc from the pointing center, no companions were detected down to a five sigma level of 10^5 $M_\odot$/channel at the center (or 1.6 10^7 $M_\odot$/channel at 45 kpc).

Table 5: Parameters derived from the H I distribution

$\alpha_{\rm adopted}$(1950)	$12^{\rm h}$ $14^{\rm m}$ $59^{\rm s}.59$
$\delta_{\rm adopted}$(1950)	$38^{\rm o}$ $4'$ $59''.7$
Position angle	-48$^{\rm o}$
Inclination	$\sim 84^{\rm o}.5$
$R_{\rm H\ I}$	11.0 kpc
$V_{\rm sys}$, heliocentric	244.4 ± 0.3 km s^{-1}
$M_{\rm tot,H\ I}$	(1.34 ± 0.07) 10^9 $M_\odot$
W_{50}	180.6 km s^{-1}
W_{20}	180.4 km s^{-1}

Notes: The adopted center of mass is derived from the total H I distribution (Sec. 3.4.). The H I -radius, $R_{\rm H\ I}$, is the radius at which the H I surface density equals 1 $M_\odot/{\rm pc}^2$. W_{50} and W_{20} are the corrected widths of the global profile at 50% and 20%, respectively, calculated according to Botinelli *et al.* (1990). .

Fig. 19 shows a composite of the high resolution ($28''.3$x$10''.1$ or 490x177 pc along the major and minor axes respectively) and intermediate resolution ($38''$x$38''$) channel maps. The data is combined such that the channels with the same speed relative to the systemic velocity are present in one frame (after having blanked those areas without emission). The receding part of NGC 4244 is the south-western part (negative X-values), the north-eastern part is approaching. The low velocity channels, which would overlap if presented in this manner, are presented individually. One local irregularity is clearly visible: the $+3'$ "hole" found in the total H I map can be seen in the frames labeled 17,18, and 19.

Each map shows a characteristic "filled V" shape. Two different mechanisms can cause such shapes. First of all it reflects the flaring of the gaseous disk. The other contributing factor is kinematic in nature: the "butterfly" pattern (seen in channel maps of less inclined systems, e.g., Bosma 1981) seen almost edge-on. In Sec. 3.5.1. I present a new method to disentangle these two effects. Classically the flaring is measured in the edge channels, i.e. at velocities of ($V_{\rm sys} \pm V_{\rm rot,max}$) (Sancisi & Allen 1979; van der Kruit 1981; Rupen 1991a).

Because of the non-flatness of NGC 4244's rotation curve the velocity edge depends on radius, so that the apparent widths can not be easily interpreted in terms of an intrinsic vertical scale height. Furthermore, systematic errors, e.g. due to non-circular motions are largest in the edge channels (Appendix 3.12.). The channels ±18 are the edge channels between about 5′ and 9′ . Here the receding side exhibits a more or less regular increase of apparent width, on the approaching side flaring is much less evident. This difference can easily arise from "local effects" (arm inter-arm surface density differences, holes, bubbles, streaming motions). The new thickness-and-inclination determination method outlined in Sec. 3.5.1. minimizes the effects of such irregularities.

A rather regular warp, starting just before the optical edge of the galaxy, is seen in the channel maps. The channels ±16,±17, and ±18 show the strongest warping at large radii. The position angle of the warp is determined by tracing the centroid of emission as a function of major axis distance. Within the optical disk, the position angle of the centroid is constant at 48° east of north. At a radius of 8′ , the position angle begins to change linearly to reach a 5° difference at 13′ . Because no clear butterfly pattern is seen in the warped region, the warp is likely to be the result of a change in position angle rather than in inclination. This is confirmed by the derived radial variation of the inclination (Fig. 27).

3.4. INFERRED PROPERTIES

In this section several properties of the gas[17] layer will be determined: the radial surface density distribution ($\Sigma_{\rm gas}(R)$), the rotation curve ($V_{\rm rot}(R)$), and the radial variation of the gaseous velocity dispersion ($\sigma_{\rm gas}$). All these quantities are required to make self-consistent predictions of the radial variation of the thickness of the gas layer (Sec. 3.6., and Chapter 2). Furthermore, with the aim to gauge the reliability of the determination of these properties, these quantities are used to compare the VLA observations with the simulated observations of NGC 4244 (Appendix 3.11.). The reader not interested in these details can skip to the next section.

Integrating the total hydrogen along the minor axis results in a major axis H I profile (Λ). The inner 4′ of this profile are symmetric about a point located $6''.9 \pm 0''.6$ to the south-west (along the major axis) of the catalogued position, which is consistent with the kinematical center. Similarly, the location of the midplane is offset by $2''.2 \pm 0''.5$ to the south-east. In the rest of this paper I assume that NGC 4244's center is located at the symmetry point of the H I -distribution: $\alpha = 12^{\rm h}\ 15^{\rm m}\ 9^{\rm s}.7$, $\delta = 38^{\rm o}\ 4'\ 59''.4$, which position is listed in Table 5. This position agrees with the kinematic center determined in Sec. 3.3.1..

3.4.1. The H I *Surface Density Distribution*

[17]Unless otherwise noted, the term "gas" refers to H I in an observational context, and to the sum of H I , H_2 and He in a dynamical context.

The mass model developed to predict the flaring of the H I layer is assumed to be axial symmetric (Chapter 2), and shows that the self-gravity of the gas contributes significantly to the vertical force. It is thus necessary to derive a reliable mean radial H I density distribution. This is done by averaging the profiles for the receding and approaching parts. In order to determine the surface density distribution, a line of sight deconvolution has to be performed.

Two different coordinate systems are useful. First there is the coordinate system centered on the center of the galaxy: (x, y, z) in Cartesian coordinates, with z the vertical coordinate and (R, θ, z) in polar coordinates (with $\theta = 0$ being the intersection of the plane of the sky with the plane of the galaxy). In the observers coordinate frame, x and d are the major and minor axes, respectively. The y-axis is parallel to the line of sight in edge-on geometry.

Assuming low optical depth (see Appendix 3.13.), the observed H I profile is an integration along the line of sight:

$$\Lambda(x) \;=\; \int_{-\infty}^{+\infty} dy\, \Sigma_{\rm gas}\left(\sqrt{x^2+y^2}\,\right) \;=\; 2\times\int_{x}^{\infty} \frac{R\,\Sigma_{\rm gas}(R)}{\sqrt{R^2-x^2}}\, dR \quad ({\rm M}_{\odot}/{\rm pc})\,. \tag{49}$$

Inversion of this Abel integral (e.g., Binney & Tremaine, 1B-59b) yields the radial surface density distribution

$$\Sigma_{\rm gas}(R) \;=\; -\frac{1}{\pi}\times\int_{R}^{\infty} \frac{1}{\sqrt{(x^2-R^2)}}\,\frac{d\Lambda(x)}{dx}\, dx \qquad ({\rm M}_{\odot}/{\rm pc}^2)\,. \tag{50}$$

This procedure can be applied at any wavelength for any inclination provided that the optical depth is low and the galaxy is not warped. Note that similar techniques were used to determine the surface brightness distribution of Virgo spirals from "pencil-beam" H I data (Warmels 1988) and the mass-to-light ratio of elliptical galaxies (i.e., Schwarzschild 1954; Binney & Mamon 1982). Adding realistic noise to a simulated spectral line cube (Appendix 3.11.) and applying Eqn. (50) yields the input $\Sigma(R)$. Thus, the derivation of the surface density distribution is not sensitive to noise. However, if the signal to noise ratio is poor, it may be preferable to use the iterative technique proposed by Warmels.

$\Sigma_{\rm gas}(R)$ is derived from a combination of the high and low resolution $\Lambda(x)$ curves and is presented in Fig. 20. Negative surface densities at small radii occur unless the $\Lambda(x)$ profile is averaged over the inner ~ 1.5 kpc. Thus this method does not recover the true $\Sigma_{\rm gas}(R, \theta)$ but it can find an azimuthally symmetric density distribution consistent with the observations: it serves as a reasonable approximation to the true distribution. Integrating the $\Sigma(R)$ profiles out to 15.8 kpc (where the surface density equals 0.02 $M_{\odot}\,{\rm pc}^{-2}$), I find 1.4 10^9 $M_{\odot}$: the Abel inversion technique conserves flux. Here I have used $\Lambda(x)$ to represent the H I profile. Because of the warp, the $x-$coordinate does not truly trace the major axis coordinate (x'). However, since x' ($=\sqrt{x^2+d^2}$) does not differ significantly for the small warp of NGC 4244

($d \leq 1$ kpc for $x \leq 13$ kpc), the derived surface density distribution is not affected by the warp.

Several strong (up to a factor 3) density enhancements ($\sim$1 kpc wide), possibly spiral arms, are present. In the inner 4 kpc the south-western and north-eastern density distributions are very similar. Beyond 10 kpc the surface density decreases in an exponential manner with a scale length of roughly 1.36 kpc. No sharp cutoff in the H I column density is observed *above* the 3σ detection limit ($5\ 10^{18}$ cm^{-2}). We see that the surface density distribution is rather symmetric (see also Sec. 3.5.2.), except in the 6 - 8 kpc region. It might be that this surface density difference is reflected in the measured flaring (Sec. 3.5.2., and Fig. 27). Because the surface densities beyond the optical disk are comparable, the contribution of the gaseous self-gravity will be similar as well, validating the use of the average surface density profile.

3.4.2. The Rotation Curve and the Velocity Dispersion of the Gas

Fig. 21 shows the intensity as a function of velocity and position along the major axis (summed over the minor axis). The rotation curve and velocity dispersion of NGC 4244 were directly derived from this plot. The maximum relative velocity outline corresponds roughly to the rotation speed minus twice the velocity dispersion in the tangential direction. The rotation speed and velocity dispersion were determined by fitting a single Gaussian to the extreme velocity envelope. These results were corrected for instrumental, line-of-sight integration, and beam smearing effects, as detailed in Appendix 3.10..

Figure 22 shows NGC 4244's smearing corrected intrinsic tangential dispersion as derived from the high, intermediate and low resolution data sets, which each sample a different range in galactocentric radius. Inside the optical disk ($R \leq 10$ kpc), the radial variation of the dispersion is quite similar to that observed in other, more face-on, systems (van der Kruit & Shostak 1982; Dickey *et al.* 1990; see Kamphuis 1993, Chap. 12, for a review). Beyond the optical disk ($R > 10$ kpc), $\sigma_{\rm gas}$ increases somewhat (from 8 to 9 km s^{-1}): similar to the small dispersion increase (from 6 to 8 km s^{-1}) seen in NGC 628 (Kamphuis 1993, Chap. 12, Fig. 1). In the other two systems where measurements of the dispersion beyond the optical disk exist, $\sigma_{\rm gas}$ declines very slowly, to 6 and 7 km s^{-1}. Thus, the radial variation of velocity dispersion in the gaseous medium of NGC 4244 is not unusual.

In Figure 23 I present the line-of-sight and beam-smearing corrected rotation curves for both sides of the galaxy. Apart from the region between 2.5 and 7.5 kpc, the rotation curves are equal to within the errors. The drop in the north-eastern rotation curve seen between 2.5 and 5 kpc is clearly a result of local phenomena (described above): there the adopted rotation curve follows the south-western curve. The 6 to 7.5 kpc region, on the south-western side, corresponds to the region where the B-band surface brightness is depressed by a factor of about 10. Therefore, I choose the intrinsic rotation curve to follow the north-eastern curve in this range of galactocentric radii. Taking these modifications into account leads to the adopted intrinsic rotation curve (indicated by the filled circles in Figure 23), which is minimally affected by non-circular motions.

Because of the large inclination, small changes thereof are not important for the derivation of the rotation curve. The maximum amplitude of the rotation velocity is about 100 km s^{-1} and starts dropping significantly beyond $R_{\rm max}$, the edge of the optical disk. At a distance of 14 kpc the rotation speed has dropped to 85 km s^{-1}. Huchtmeier (1975) finds, using a $9'$ beam, that the H I extends out to $18'$ and determines a rotation speed of 85 ± 5 km s^{-1} at that distance. The measurements presented in this paper do not confirm this detection. The symmetry between the two sides indicates that the gas is likely to be on circular orbits, except for the regions mentioned above. The symmetric drop in rotation curve on both sides of the disk is the strongest argument that we are actually measuring the circular velocity and that this drop is not caused by, for example, a lack of gas on the major axis: an explanation which has been invoked to explain asymmetric drops seen in other edge-on galaxies (Sancisi & Allen 1979).

3.5. THE DETERMINATION OF THE THICKNESS OF THE HYDROGEN LAYER

In the past, the radial increase of the thickness of the gas layer has been determined from apparent width measurements of the edge channels only (Sancisi & Allen 1979; van der Kruit 1981; Rupen 1991a). The main advantage of this procedure is that the edge channels select a region (the "emitting region") around the major axis which is relatively narrow, so that its width, as projected onto the sky, does not contribute much to the observed apparent thickness. This procedure has two disadvantages however: 1) the magnitude of the projection effect depends strongly upon inclination, e.g., at i=85^{o} it varies by a factor of two for an inclination difference of 2^{o} , and 2) only two points per galactocentric radius, one on the approaching side and one on the receding side, are measured.

Irwin & Seaquist (1991) modeled the entire spectral line cube obtained for NGC 3079 to obtain the rotation curve, surface density distribution and gas layer width (assumed a constant with radius). Braun (1991) devised a technique to determine the inclination and the thickness of the gas layer for M31, where the H I emission is found primarily in the spiral arms. The method presented here works best if the H I is distributed smoothly.

Below I describe a new method to simultaneously determine the inclination and the thickness of the gas layer of external galaxies. As the essence of this method is to utilize data from many azimuths (channels), both disadvantages of the edge-channel procedure are circumvented. This is accomplished by modeling the contribution of the emitting region. Two aspects are crucial: 1) the emitting region can be well modelled if the rotation curve is known, for example for a flat rotation curve a channel of a $\Delta V_{\rm chan}$ km s^{-1} wide is sensitive to gas in a wedge-like region in the plane of the galaxy (Sancisi & Allen 1979, their Fig. 6), where the width of this emitting region follows directly from the rotation curve, the channels velocity and the channel width, and 2) for a given galactocentric radius the width of the emitting region varies systematically with azimuth (observing frequency, or velocity). Thus the projected width of the emitting region also varies systematically with radius in a manner which can be described exactly for a given observed rotation curve and channel width. These projection effects can be clearly seen in Fig. 8 of Sancisi & Allen, where the apparent width of the gas layer is larger in those channels whose velocities are closer to the systemic velocity. The apparent thickness of the gas layer is then the sum of the projected vertical thickness of the gas layer and the projected planar width of the emitting region. Only two unknowns (the vertical thickness and the inclination) are involved. Since the apparent widths can be measured at many azimuths, and the planar width of the emitting region can be calculated as a function of galactocentric radius and azimuth, the inclination and vertical thickness of the gas layer can be simultaneously determined from measurements of the apparent thickness in many channels.

3.5.1. Outline of the Method

The method outlined below works for a more realistic situation where the rotation curve is not flat and where the gaseous velocity dispersion softens the edges of the wedges. A more detailed description is given elsewhere (Olling 1995b).

In the case a galaxy is not edge-on, the azimuthal dependence of the flaring might determined by measuring the apparent thickness (in a given velocity channel) along an ellipse with axial ratio $1/\cos i$. In close to edge-on observing geometry this procedure is complicated by the intrinsic thickness of the gas layer, while at $i = 90^{\circ}$ this methods fails altogether. However, at any inclination, the galactocentric radius (R) can be determined from the rotation curve ($V_{\rm rot}$), the major axis position[18] (x) and the observing velocity ($V_{\rm chan}$):

$$R \;=\; \frac{x}{\cos\theta} = x\,\frac{V_{\rm rot}(R)\;\sin i(R)}{\mid V_{\rm chan} - V_{\rm sys}\mid} = x\,\frac{V_{\rm proj}(R)}{\mid V_{\rm chan} - V_{\rm sys}\mid}\,, \tag{51}$$

with $i(R)$ the inclination, and $V_{\rm sys}$ the galaxy's systemic velocity. It is important to realize that the determination of R depends on the projected rotation speed (i.e. the *product* of $V_{\rm rot}(R)$ and $\sin i(R)$) which is, at any inclination, much better determined than the individual quantities: the kinematic determination of R is robust[19]. When the apparent widths in a given channel are determined, Eqn. (51) is used to assign a galactocentric radius to the measurements obtained at major axis position x. For a given channel and major axis position, the width of the emitting region can be determined as well, so that the apparent width measurements can be corrected for inclination and projection effects to yield the intrinsic thickness of the gas layer. Below I describe how the width of the emitting region can be determined.

---

[18]The coordinate system is defined in Sec. 3.4.1..

[19]The effects of non-circular motions are discussed in Appendix 3.12..

Rather than using the wedge-approximation discussed in the previous section, I include the effects of the velocity dispersion of the gas, the exact shape of the rotation curve, and the gaseous surface density distribution to determine the size of the emitting region. Given these parameters, which have been determined independently in the previous sections, it is easy to calculate[20] what fraction of the column density has a projected velocity equal to $(V_{\rm chan} \pm \frac{1}{2}\Delta V_{\rm chan})$, for all points in the galaxy (Olling 1995b). These channel surface density distributions ($\Sigma_{\rm chan}(x, y; V_{\rm chan})$, hereafter referred to as CSDDs) are the more rigorously calculated equivalent of the wedge-like emitting regions described above. Some CSDD maps are presented in Fig. 24. Alternatively, one could think of a CSDD as a deprojected (to face-on view) channel map of an infinitely thin gas layer. A rough idea about the shape of the CSDDs can be formed by deprojecting (to face-on view) a velocity field which is contoured at $MAX(\Delta V_{\rm chan}, \sigma_{\rm gas})$ km s^{-1} intervals. But note that a CSDD is neither a deprojected channel map[21], nor a deprojected velocity field. Along a line perpendicular to the major axis, the shape of the emitting region is no longer discontinuous, but can be parameterized, to reasonable accuracy, by two Gaussians:

$$\Sigma_{\rm C}(y; x, V_{\rm chan}) \;\propto\; \left(e^{-\frac{1}{2}((y-Y_{\rm C})/W_{\rm C})^2} \;+\; e^{-\frac{1}{2}((y+Y_{\rm C})/W_{\rm C})^2}\right) , \tag{52}$$

one for the near side and one for the far side. Non-linear least squares fits to the profiles yield typical errors of 0.5% - 1.5% and 0.2% - 0.6% for $W_{\rm C}$ and $Y_{\rm C}$, respectively. As the CSDDs are different for each channel, so are (for a given galactocentric radius) $Y_{\rm C}$ and $W_{\rm C}$, which depend mainly on the rotation curve and the gaseous velocity dispersion, respectively. Projecting the CSDD onto the sky, the apparent planar width is given by:

$$\cos i \; FWHM_{\rm p}(x; V_{\rm chan}) \;\approx\; 2.35 \cos i \sqrt{W_{\rm C}^2(x; V_{\rm chan}) + [Y_{\rm C}(x; V_{\rm chan})]^2} , \tag{53}$$

where the $Y_{\rm C}$-term is only included when the projection of near and far side of the CSDD are unresolved by the beam, i.e. in nearly edge-on viewing geometry. Since the vertical density distribution of the gas is approximately Gaussian (Paper I), and the planar distribution of the CSDD resembles a double Gaussian (Eqn. [52]), the line-of-sight integration through this density distribution is approximately (double) Gaussian as well. The observable width, convolved with the synthesized beam ($FWHM_{\rm b}$), is given by:

$$\begin{aligned} FWHM_{\rm obs}^2(x; V_{\rm chan}) \;=\; & [FWHM_{\rm z}(R) \sin i(R)]^2 + [FWHM_{\rm p}(x; V_{\rm chan}) \cos i(R)]^2 + \\ & FWHM_{\rm b}^2 , \end{aligned} \tag{54}$$

[20] The Channel Response Function appropriate for these VLA observations is used (see Appendix 3.10.).

[21] One can easily convince oneself of this by stretching the d-coordinate (by 1/cos(85°)) of some channel maps as presented in Fig. 19 and compare them with the CSDD maps in Fig. 24.

Using this equation, a fit to the measured apparent widths in many channels yields the intrinsic thickness and the inclination of the gas layer. The required values for $FWHM_{\rm p}(x;V_{\rm chan})$ are determined from the CSDD maps. In each channel map (and CSDD map) the major axis distance x is chosen such that the same galactocentric radius is sampled [via Eqn. (51)]. I solve Eqn. (54) using a non-linear least squares technique[22] which also yields the errors on i and $FWHM_{\rm z}$. For the case of NGC 4244, typically 12 measurements of $FWHM_{\rm obs}$ are used. The square of the difference between the observed and model widths is minimized by varying the inclination and gaseous width, where each data point is weighed by the square of the inverse of its error. The error on each data point is calculated by adding (in quadrature) the error in the right-hand side of Eqn. [54], as calculated from the error in i and $FWHM_{\rm p}$, to the observational error. Since the contribution from the right-hand side depends on the exact value of the inclination, several iterations are required.

For less inclined systems, inclination and thickness can be determined from each channel individually using

$$\cos i(R;V_{\rm chan}) = \frac{\Delta d(R;V_{\rm chan})}{2Y_{\rm C}(R;V_{\rm chan})}\,, \tag{55}$$

and

$$FWHM_{\rm z}^2(R;V_{\rm chan}) = \frac{FWHM_{\rm obs}^2(R;V_{\rm chan}) - FWHM_{\rm b}^2 - [2.35W_{\rm C}(R;V_{\rm chan})\cos i(R)]^2}{\sin^2 i(R)}\,, \tag{56}$$

where Δd is the projected separation of the two “wings” of the “butterfly” (e.g., see Paper I, Fig. 13). From the inclination and thickness values determined from the individual channels the weighted averages are calculated, where the weights are the inverse of the square of the errors. The errors in the right hand sides of Eqns. (55) and (56) include the errors on d, $FWHM_{\rm obs}$, $Y_{\rm C}$, $W_{\rm C}$ and i.

Previous workers (Sancisi & Allen 1979; van der Kruit 1981; Rupen 1991a) corrected their edge channel flaring determinations for these projection effects, but made no effort to model the emission in lower velocity channels in detail. However, as we have seen, the lower velocity channels hold the key to the simultaneous determination of flaring and inclination. Furthermore, since many azimuths (channels) are used, the effects of local irregularities are reduced.

Both the intrinsic thickness of the gas layer and the width of the CSDD increase approximately linearly with radius: the former because of the $1/R^2$ DM-halo density

[22] The performance of a least squares technique can be greatly improved by imposing physical limits on the to be fitted parameters. For example I restrict the inclination to lie in the range $0^{\rm o}$ -$90^{\rm o}$, and the thickness of the gas layer to be positive. A standard LSQ routine (e.g. MRQMIN, Press *et al.* 1990) can be easily modified to include physical limits in the step where a new guess for the solution is calculated: if the new guess exceeds a physical boundary, then the new guess is placed halfway between the old guess and the physical boundary.

distribution (Paper I), the latter because of the fact that a channel of a certain velocity width is sensitive to gas in a wedge of constant opening angle. Simple analytic considerations (Olling & van Gorkom 1995[23] ; Olling 1995b, Chapt. 4) indicate that the ratio of these two projected widths depends strongly on inclination and only weakly on the properties of the galaxy. For a typical channel, the projected gas layer width exceeds the projected CSDD width for inclinations larger than about 60 degrees. This inclination cutoff is confirmed using "observations" of simulated galaxies seen at various inclinations (Fig. 25). Thus it is expected that for galaxies with inclinations exceeding 60° the flaring, and hence the DM-halo flattening, can be determined.

3.5.2. The Thickness of NGC 4244's Gas Layer

In Fig. 26 I present the measurements of the apparent thickness for some channels (± 8,± 10,± 12,± 14,± 16,± 18,± 20) used in the determination of inclination and thickness of the gas layer. The peak of the fitted Gaussians at each radius is plotted in the two outer panels, the apparent thickness in the inner panels. At each radius only those profiles with at least three independent points larger than four times the local noise are included. The asymmetries in the surface density profile (Fig. 20) at 5.5 kpc and 6-8 kpc can be seen in many of the individual channels: in agreement with the surface density profile derived with the Abel inversion technique. Generally, the profiles are well represented by a single Gaussian. Two-component fits were attempted as well. A reliable two-component fit must satisfy the following criteria: a) the amplitudes of the components may not differ by more than 60%, b) the components must have equal widths, c) the separation between the components must exceed $MAX(FWHM_{\rm b}, 0.77 \times FWHM_{\rm cmp})$, and d) its goodness of fit[24] must exceed the goodness of fit of the one-component fit. As a result of these stringent criteria, only at a few locations reliable two-component fits could be made. The four-σ criterion applied restricts thickness measurements to regions where the face-on surface density exceeds about 2 10^{19} cm^{-2}.

Since at most locations no reliable two-component fit can be made (see Fig. 26), the thickness and inclination are determined using Eqn. (54). The results are presented, for the two sides of the galaxy, in Fig. 27. The radial variation of thickness in the upper panel, the inclination in the lower panel. The plot on the left-hand side results if the inclination is a free parameter, while fixing the inclination leads to the thickness determinations plotted on the right.

Using the observational errors only, the reduced χ^2 values of the fits [to Eqn. (54)] are of the order of 3.5 (± 1.5) for radii smaller that ∼ 8 kpc and increase sharply to ∼ 13 (± 7) beyond. This indicates that either the model is bad or that the errors have been

[23]Notice a typo in their Eq. (4): $\sigma_z(R)$ has to be replaced by $\sigma_z(R) \times R$

[24]$Q(\nu, \chi^2) \equiv \Gamma(^1/_2\nu,\ ^1/_2\chi^2)/\Gamma(^1/_2\nu)$, with ν the number of degrees of freedom and χ^2 the sum of the noise-normalized square of the difference between model and data points (see Press *et al.* 1990, Chapt. 14).

underestimated. In Appendix 3.12. I show that non-circular motions contribute to the error budget of Eqn. (54) as well. The inclusion of errors associated with non-circular motions ($\sim$ 2 km s^{-1} for $R \leq 8.5$ kpc and ~ 8 km s^{-1} beyond) decreases the reduced χ^2 to values around one. The onset of the warp around 8.5 kpc suggests that modest non-circular motions are associated with the warp.

The beamsize corrected widths from the high (177 pc) and intermediate (665 pc) resolution are generally equal to within the errors, which indicates that the width measurements are not hampered by resolution effects. The flaring determination in the inner five kpc is less reliable because errors arising from kinematical distortions are approximately inversely proportional to the local rotation velocity [Eqn. (76)]. Thus non-circular motions can have large effects in the inner 5 kpc, so that it is not advisable to use this region to draw inferences about he mass-to-light ratio of the stellar disk. The derivation of the halo's flattening is not affected.

Another problem area may be the 7 - 8.5 kpc hump on the south-western side, where the thickness of the gas layer is 70% larger, and the gaseous surface density distribution (Fig. 20) 50% lower than on the north-eastern side. The stellar surface density is possibly smaller (approximately by a factor of ten) on the south-western side as well (Sec. 3.2. and Fig. 16). In the outer part of the optical disk the self-gravity of the gas can contribute significantly to the vertical force (see Paper I, Fig. 10). In the case of NGC 4244 models which include the gaseous self-gravity have gas layer widths 50% smaller than models which do not, between 6 and 10 kpc. Therefore I plot the north-eastern rather than the average flaring curve from 6 to 8.5 kpc in Fig 29.

From these flaring measurements taken at different resolutions and sensitivities I extract two flaring curves, one for the varying inclination case, the other for the fixed inclination case. For radii between 6 and 10 kpc I use the flaring data extracted from a 357-pc (minor axis) resolution data set. The high (177 pc) and intermediate (665 pc) resolution flaring results are used for the regions smaller than six and larger than ten kpc, respectively. The "errors" are either the error on the average of the two sides, or, if larger, half the difference between the two values, so that the *systematic* differences are reflected by the extent of the error bars.

3.6. THE MASS MODEL

The dependence of the thickness of the gas layer upon the shape of the dark matter halo is described in Chapter 2. Here I like to present four of the most salient features. That the thickness of a gas layer depends on the axial ratio ($q_\rho = c/a$) of the halo can be easily understood. For an axisymmetric ellipsoidal dark matter distribution with fixed $R_{\rm c}$ and ρ_0, [like Eqn. (57)] the mass enclosed by an ellipsoid of axial ratio q_ρ, and hence the rotation speed, decreases with decreasing q_ρ. Thus, for a given observed rotation curve, the densities of flattened halos have to be larger than in a round halo . The vertical force, proportional to the mass enclosed (Gauss' theorem), increases as well so that a thinner gas layer results. The second important result obtained in Chapter 2 is that the mass-to-light ratio (or equivalently, the mass) of the stellar disk has virtually no influence on the thickness of the gas layer beyond the stellar disk. Given the fact that the dark matter density distribution is poorly known (van Albada *et al.* 1985; Lake & Feinswog 1989; Chapter 2) this may seem surprising at first. However, close to the plane the vertical force[25] is roughly proportional to the radial force which is, by construction, the same for all disk-halo combinations that reproduce the observed rotation curve. Thirdly, the self-gravity of the gas contributes significantly to the vertical force. And finally, the model gas layer widths are best calculated using the global approach, in which the vertical force is determined from the global mass distribution of the galaxy.

Comparing the thickness measurements beyond the optical disk with model flaring curves, calculated for a series of mass model with varying halo flattening, yields the flattening of the DM halo. Input to these mass models are the observed rotation curve, the density distributions of the dark and luminous matter and the gaseous velocity dispersion[26]. Below I describe how to arrive at these density distributions.

Optical studies of edge-on spiral galaxies indicate that the z scale height of the disk is constant as a function of galactocentric distance (van der Kruit & Searle 1981a,b 1982a,b; Barteldrees & Dettmar 1994), although there are theoretical and observational indications that the shape of the vertical distribution may change with radius (Burkert *et al.* 1992 and van Dokkum *et al.* 1994, respectively). Here a constant vertical scale height is assumed. For the vertical distribution I use an exponential as well as a $\mathrm{sech}^2(z/z_0)$ distribution. The effects of a different choice for the vertical stellar distribution are discussed in Sec. 3.7.4.. To avoid extinction features (Fig. 16), a fit to the stellar radial surface brightness distribution is used: $L(R) = L(0)\exp(-R/h_\mathrm{R})$ for $R \leq 10$ kpc, followed by a linear decline till 11 kpc and $L(R) = 0$ beyond 11 kpc. A constant mass-to-light ratio ($M/\mathcal{L}$) is assumed. The stellar density distribution is thus given by the product of the mass-to-light ratio and the assumed radial and vertical distributions.

The gaseous surface density used is the sum of the H I surface density distribution displayed in Fig. 20, a crude estimate of the H_2 surface density distribution (Sec. 3.2.), and 25% He by mass. The volume density is found from $\Sigma_\mathrm{gas}(R)$, σ_gas and the total potential, via the equation of hydrostatic equilibrium. Details of this procedure can be found in Chapter 2. A Gaussian fit to this density distribution yields the model gas layer widths [see footnote 4 in Chapter 2]. In Sec. 3.6.1. these model widths will be compared to the measured flaring curve.

The dark halo volume density is parameterized as a flattened isothermal sphere with

---

[25] $K_\mathrm{z} = z/\sqrt{z^2+R^2}\, F_\mathrm{tot} \approx z/R\, F_\mathrm{R} \propto \frac{z}{R}\, V_\mathrm{obs}^2$

[26] It is assumed that the velocity dispersion in the gas is isotropic, i.e., that the vertical velocity dispersion equals the measured tangential velocity dispersion.

core radius $R_{\rm c}(q_\rho)$, central density $\rho_0(q_\rho)$, and flattening $q_\rho(= c/a)$ (e.g., Sackett & Sparke 1990; Sackett *et al.* 1994; Chapter 2):

$$\rho(R, z; q_\rho) \;=\; \frac{\rho_0(q_\rho)\, R_{\rm c}^2(q_\rho)}{R_{\rm c}^2(q_\rho) + R^2 + (z/q_\rho)^2} \;. \tag{57}$$

The dependency of $R_{\rm c}$ and ρ_0 upon q_ρ is such that the rotation curve of any flattened density distribution described by Eqn. (57) is practically indistinguishable from its round equivalent (Chapter 2). In the flat rotation curve regime, the thickness of the gas layer in a density distribution like Eqn. (57) is given by:

$$FWHM_{\rm z}(R) \;\approx\; 2.35 \left(\frac{\sigma_{\rm gas}}{V_{\rm rot,max}}\right) \sqrt{\frac{2.4\, q}{1.4 + q}}\; \sqrt{R^2 + {R_{\rm c}}^2} \;, \tag{58}$$

with $V_{\rm rot,max}$ the asymptotic rotation speed of the DM halo [Eqn. 45].

The mass models described above are fully specified by two free parameters, the stellar mass-to-light ratio and the flattening of the DM halo. For every choice of the stellar $M/\mathcal{L}$, the DM core radius and central density are uniquely determined by the shape of the observed rotation curve (Chapter 2). By taking the mass-to-light ratio of the stellar disk as a free parameter the problems involved with decomposing the observed rotation curve in luminous and dark matter parts (van Albada *et al.* 1985; Lake & Feinswog 1989) are avoided. Note that the shape of the DM halo is not a parameter in such disk-halo decompositions (see above and Chapter 2 I).

In Fig. 28 (upper panel) I present the observed rotation curve and some model curves which span the allowed range in $M/\mathcal{L}_{\rm B}$. Recall that the observed rotation curve is less accurately determined between 2.5 and 7.5 kpc (Sec. 3.4.2.). These disk-halo models are fully specified by model rotation velocities at two points (at $2.3h_{\rm R}$ and $8h_{\rm R}$) and $M/\mathcal{L}$. From those three parameters the the DM-halo's core radius and central density are uniquely determined (Chapter 2 I). Rather than determining best values for these parameters from a fit to the observed rotation curve, I estimate the model rotation speeds at $2.3h_{\rm R}$ and $8h_{\rm R}$ for which the largest possible range in $M/\mathcal{L}$ yield acceptable overall correspondence between the model and observed rotation curves. The observed rotation speeds at these points are good initial estimates for those model rotation speeds. The slow rise of the rotation curve in the inner five kpc, and the decline beyond the optical disk limits $M/\mathcal{L}_{\rm B}$ to the range 3.1 - 6.2. The DM-halo parameters are not well constrained, possible core radii range from 0.3 to 12 kpc and central densities between 1 and 0.002 $M_\odot/{\rm pc}^3$ are allowed: small $M/\mathcal{L}$'s correspond to small core radii and large halo densities (Chapter 2, Fig. 3). Because of the falling rotation curve, only a small amount of dark matter is required: 1.1 times the luminous mass for the maximum disk case, and 2.6 times the luminous mass for the half-maximum disk case.

Again, notwithstanding this enormous allowed range in halo parameters, the thickness of the gas layer in such disk-halo models (with the same flattening) is very similar (Fig. 29).

3.6.1. The Shape of the Dark Halo

Finally we can compare the calculated gas scale heights for several mass models with various $M/\mathcal{L}$ and q_ρ with the observed widths (Fig. 29). The truncation of the stellar disk, the gaseous self-gravity and the measured gaseous velocity dispersions (Fig. 22) have been included in the model calculations.

Inspecting this figure we notice general correspondence between the observations and the model flaring curves, except for the 7 kpc hump. Here the thickness of the gas layer increases by a factor 2.7 within 1 kpc (on both sides of the galaxy). Similar features are seen in the Milky Way (Knapp 1987) and NGC 891 (Rupen 1991a) but are absent in NGC 4565 (Rupen 1991a). The steep thickness gradients in NGC 891 and NGC 4244 seem to occur just inside and just outside H I surface density enhancements. Such sudden changes in apparent thickness can arise from streaming motions induced by spiral structure (see Appendix 3.12.).

Both the maximum-disk and the minimum-disk model curves seem to represent the flaring data equally well (upper and lower panel, respectively). This is corroborated by the fact that the largest reduced χ^2 lies within the 1-σ bound (i.e., $\chi^2 \leq \chi^2_{\rm min} + 1$) of the model with the smallest reduced $\chi^2_{\rm min}$. The north-eastern, sout-western, and the average flaring curves all yield the same estimate for the mass-to-light ratio. Thus, for NGC 4244, the measured flaring does not constrain the mass-to-light ratio of the stellar disk beyond the limits set by the shape of the rotation curve.

On the other hand, the flattening of the halo is much better constrained. For all stellar disk masses, the minimum χ^2 is found at the same halo flattening, with the same formal uncertainty. The uncertainty in the inclination determination in the outer parts of the galaxy (Sec. 3.5.2.) has only a small effect on the inferred DM-halo shape: for the varying-inclination case I find q_ρ=0.2 $\pm$ 0.1, the fixed-inclination case yields q_ρ=$0.3^{+0.2}_{-0.1}$. There are several reasons why I believe that the small decrease in inclination beyond the optical disk is probably real: 1) it is seen on both sides of the galaxy, 2) it is seen (with lower S/N) when using the low velocity channels (8-14) only, as well as in the “edge” channels (15-20) only. I thus discard the fixed-inclination solution.

3.7. CAVEATS

We have seen that the dark halo of NGC 4244 is significantly flattened. Below I discuss the main uncertainties in this result.

3.7.1. The Gaseous Velocity Dispersion

Like the surface density, the velocity dispersion of the gas is an important parameter in the analysis presented above: the calculated thickness of the gas layer and the inferred halo flattening depend, respectively, linearly and quadratically on the velocity dispersion of the gas (Chapter 2.3.5): from Eqn. (58) it follows that $FWHM_{\rm z}^2 \propto {\sigma_{\rm gas}}^2\, q_\rho$. This strong dependence in illustrated in Fig. 30, where I compare model gas layer widths calculated for the lower and upper bounds to the gaseous velocity dispersion found in other, more face-on, systems (van der Kruit & Shostak 1982; Dickey *et al.* 1990; see Kamphuis 1993, Chap. 12, for a review). It is striking that the shape of the halo can not be determined if no velocity dispersion measurements are available: measuring the gaseous velocity dispersion is instrumental in the determination of the shape of the dark matter halo.

From Fig. 31 we can see that forcing the flaring measurements to be consistent with a round DM-halo model requires a radial decline of the velocity dispersion which is inconsistent with the dispersion measurements. However, in Sec. 3.6. the assumption was made that the vertical velocity dispersion ($\sigma_{\rm zz}$) equals the measured tangential dispersion ($\sigma_{\theta\theta}$). The measured tangential dispersion curve can thus be consistent with round DM halo if ($\sigma_{\rm zz}/\sigma_{\theta\theta}$) decreases radially (down to 0.55 at the last measured point). At the present time it is unclear whether such a large anisotropy in the gas is consistent with the observations. For the molecular component of the Milky Way this ratio is observed to equal 0.7 ± 0.4, at the solar radius ($\sigma_{\rm zz} = 5.7 \pm 1.2$ for high latitude CO clouds, Blitz *et al.* 1984; $\sigma_{\theta\theta} = 7.8 \pm 4$ from tangent point measurements, Malhotra 1994).

In Appendix 3.10. I show that a 10% over estimate of the measured dispersion is possible, but only so if the dispersion *increases* by more than 50%/kpc along the line of sight. Such an increase along the line of sight seems hard to reconcile with the radially decrease required to infer rounder halos. Note that the up to radii of 14 kpc the signal-to-noise ratio is large enough (≥ 10) to determine the dispersions reliably.

3.7.2. The Determination of the Inclination

Because the inferred halo flattening is proportional to the square of the true width of the gas layer [Eqn. (58)], the thickness of the gas layer has to be measured reliably. It must be stressed that the inclination is a critical parameter for determining the intrinsic thickness of the gas layer. This is so because, at inclinations around 85$^{\rm o}$ a large part of the apparent width arrises due to the projected separation of the CSDD wings (Sec. 3.5.1.), which changes by 40% between 85$^{\rm o}$ and 83$^{\rm o}$. The simultaneous determination of inclination and thickness is thus instrumental in the process of determining the shape of the DM halo. The small difference in the inferred q_ρ between the thickness for the fixed-inclination solution and the free-inclination solutions falls within the range allowed by the uncertainty in the gaseous velocity dispersion.

3.7.3. Non-circular Motions

The assumption of circular orbits is basic to the thickness determination method presented in this paper. Closed orbits of ellipticity $\epsilon_{\phi,\rm p}$ may exist in such a potential. In an elliptic logarithmic potential the radial and tangential velocity can be found analytically [e.g., Rix & Zaritsky 1995, their Eqns. (7) and (8)]. As a result, the difference between the observable *recession* velocities of an elliptical disk and a circular disk have a period of $\pi/3$ and an amplitude of $\epsilon_{\phi,\rm p} V_{\rm rot}$. With θ_ϕ the direction of the major axis of the potential, the observable velocity difference between two points at (R, θ) and $(R, -\theta)$ equals zero and $(2\epsilon_{\phi,\mathrm{p}} V_{\mathrm{rot}} \sin(2|\theta_\phi|))$ for a round disk and an elliptical disk, respectively. For ellipticities as reported by Rix & Zaritsky ($0.045^{+0.03}_{-0.02}$), the effects of elliptical orbits are smaller than 9 km s^{-1}, so that the determination of the flaring is not affected much. The measured recession velocity on the major axis equals $V_{\mathrm{sys}} \pm V_{\mathrm{rot}}(R)\,\{1 + \epsilon_{\phi,\mathrm{p}} \cos(2\theta_\phi)\}$. Given the predicted and measured upper limits to $\epsilon_{\phi,\mathrm{p}}$, ($\leq 0.1$, Dubinski 1994; and ≤ 0.075, Rix & Zaritsky 1995), the measured 15% decrease in rotation speed can not be explained by a rapid radial variation in ellipticity or location of major axis of the dark matter distribution.

3.7.4. The Stellar Mass Distribution

Since the shape of the DM halo can be determined irrespective of the actual mass of the stellar disk, its vertical distribution is unimportant as well. However, the shape of the vertical distribution of the stars determines the mass-to-light ratio of the stellar disk.

Van der Kruit & Searle (1981a) determined the central surface brightness assuming a $\mathrm{sech}^2(z/z_0)$ vertical light distribution. However, it has been argued that the intrinsic vertical distribution is exponential and that the $\mathrm{sech}^2(z/z_0)$ distribution results from dust extinction (e.g., Wainscoat *et al.* 1989), in which case the face-on surface brightness is twice larger. This exact argument only holds for edge-on systems and only if the low-z measurements are thought to be unreliable. Thus the radius at which the face-on surface brightness equals 25 mag/$\square''$ differs for the two vertical distributions as well. Using the correlation between D_{25} and the H I -radius (Broeils 1992, Chap. 3) neither vertical distribution can be ruled out.

The stellar mass required for a given disk-halo decomposition of the rotation curve depends somewhat on the vertical distribution of the stars (Casertano 1983). Therefore, a vertically exponential disk has a mass-to-light ratio approximately twice smaller than a vertically sech^2 disk (van der Kruit 1988). Thus, for either vertical distribution the range in possible mass-to-light ratios correspond to 50% - 100% of the maximum-disk value.

The fact that the inferred mass-to-light ratio for the maximum disk case (6.2) is about twice as large as typical for an Scd galaxy (Broeils 1992, Chap. 10), suggests that the vertical distribution is exponential rather than sech^2, or that the stellar disk is actually less massive than maximum-disk. Additional information regarding the vertical structure of the stellar disk is required to determine the stellar mass more accurately.

In Sec. 3.6. it was assumed that the stellar mass-to-light ratio is constant throughout the galaxy. As argued above, a vertically varying mass-to-light ratio does not affect the inferred halo flattening.

A radial gradient in the stellar $M/\mathcal{L}$ would change the radial distribution of stellar mass. Consider the case that the radial scale length changes, this would expand the horizontal scale of the *predicted* flaring curves (Fig. 29) by $h_{\mathrm{R,true}}/h_{\mathrm{R,false}}$, while the measured flaring remains unchanged. Thus, given an observed flaring curve, flatter DM halos are inferred for shorter true radial scale lengths. In many systems the scale length as determined from near-infrared photometry is significantly shorter than the scale length at visual wavelengths (Terndrup *et al.* 1994; Peletier *et al.* 1994), Extinction can not be the sole reason for this radial blueing since such color gradients are found in face-on systems as well (de Jong & van der Kruit 1994; de Jong 1995). In fact, it may be that a radially varying star formation history (mean stellar age) in combination with a radial metalicity gradient cause the observed color gradients (de Jong 1995, Chapter 4). However, such color gradients are small[27] for late type, low luminosity systems like NGC 4244. Since extinction is not very important (Sec. 3.2.) in NGC 4244 and the current star formation is low (Sec. 3.2.), the measured blue light probably traces mass, so that the inferred DM-halo flattening is probably unaffected.

3.7.5. Distance Dependence

When combining the Eqns. (44) and (eq:MoverL.versus.gamma) from Chapter 2, it follows that the model thickness, inside the stellar disk, is proportional to $\sqrt{h_{\rm R} z_{\rm e}}$, equivalent to a linear distance dependence. Likewise, the the thickness of the gas layer beyond the optical disk is linearly proportional to galactocentric radius, thus depending linearly on distance. As the thickness measurements also depend linearly on distance, the flaring gas layer method yields distance independent values for the mass-to-light ratio of the stellar disk and the shape of the DM halo.

3.7.6. The Influence of the Extragalactic Radiation Field

The major axis H I surface density profiles of NGC 3198 (van Gorkom 1993) and M33 (Corbelli *et al.* 1989) show sudden change in slope at column densities below a few times 10^{19} cm^{-2}. Maloney (1993) interprets these slope changes as evidence for the presence of an extragalactic radiation field ionizing the neutral hydrogen layer. Another effect of such a radiation field is to decrease the width of the *neutral* gas layer at column densities below about 7-12 10^{19} cm^{-2}, or volume densities below 0.0085 - 0.017 cm^{-3} (Maloney 1993, his Fig. 7), for one-sided ionizing fluxes of 1 - 7 10^4 ionizing photons cm-2 s^{-1}, respectively. The current 2-σ upper limit for the metagalactic radiation field is 3 10^4 cm-2 s^{-1} (Vogel *et al.* 1995). The azimuthally averaged surface density profile of NGC 4244 (Fig. 20) shows a change in slope at a column density of $\sim 10^{20}$, which would occur for a metagalactic radiation field stronger than the current upper limit (Vogel *et al.* 1995). The surface and the volume densities of NGC 4244 are such that a metagalactic radiation field of 1 10^4 cm-2 s^{-1} would affect the thickness of the gas layer by less than $\sim 10\%$ for radii less than 13 kpc. Where the flux as large as the current observational 2-σ upper limit, the true thickness of the gas layer may be 15% larger at 12 kpc. In that case, the metagalactic radiation field could have an effect on the inferred halo flattening of the same order of magnitude as the uncertainties in the gaseous velocity dispersion and the inclination.

The inferred halo flattening is thus unaffected.

[27]There are twelve systems in de Jong's (1995) sample which are comparable to NGC 4244: in scale length, total luminosity and total H I mass. For those systems I find $h_{\rm K-band}/h_{\rm B-band} = 1.02 \pm 0.06$, corresponding to small color gradients.

3.7.7. Non-Thermal Pressures

The analysis presented in this paper assumes the vertical gravitational force is balanced by thermal pressure only. It is estimated that in the solar neighborhood the pressures due to cosmic rays and magnetic fields are of comparable magnitude (Spitzer 1978, p. 234). The magnetic field of the Milky Way has a very long radial scale length (Kulkarni & Heiles 1988, p. 146) and could provide significant pressure, even beyond the optical disk. However, such a stratified magnetic field is unstable (Parker 1966) and may not contribute to the vertical pressure balance. Non-thermal radio emission indicates that cosmic rays are closely related to sites of star formation (Bicay & Helou 1990), and do not extend much beyond such regions. With the radio continuum flux very low (Sec. 3.2.) it is expected that cosmic ray pressure contributes little to the total pressure, especially beyond the optical disk. In the Introduction I summarized observational evidence against the importance of non-thermal pressures (Rupen 1991a). At any rate, if non-thermal pressures *are* important, then an even larger DM-halo midplane density is required to produce the observed flaring: additional non-thermal pressures require an even flatter DM halo (see also Pfenniger *et al.* 1994, and references therein).

3.8. DISCUSSION

The thickness of the gas layer has been measured for only a few galaxies: The Milky Way (e.g., Kulkarni *et al.* 1982; Knapp 1987; Wouterloot *et al.* 1990; Merrifield 1992; Malhotra 1994, 1995), NGC 891 (Sancisi & Allen 1979; van der Kruit 1981; Rupen 1981a), NGC 4565 (Rupen 1991a), and M31 (Braun 1991). The rapid variations (up and down by a factor of 2 - 4 within 500 pc) in the thickness of the gas layer of NGC 891 (Rupen 1991a) are probably caused by spiral arm streaming motions which change the shape of the edge channels (see also Appendix 3.12.). Inside the stellar disks, the thickness ($FWHM$) of the gas layer increases gradually from $\sim$150 pc to $\sim$800 pc at the edge of the stellar disk, similar to the flaring of NGC 4244 as determined in this paper.

The gas layer width increases exponentially with radius if the potential is dominated by the stellar disk (e.g., van der Kruit 1988; Chapter 2). For this reason, most authors fit exponential functions to the observed flaring curves and use simple models for the potential of the galaxy to derive that the stellar mass-to-light ratio is roughly constant with values between 50 and 100% of the maximum disk value (van der Kruit 1981; Rupen 1991a). A more detailed model of the potential, like the one described in Chapter 2, could be used to re-analyse these data sets. However, in order to improve upon the current $M/\mathcal{L}$ estimates, both the vertical stellar distribution, and the gaseous velocity dispersion need to be accurately determined.

With the edge of the stellar disk of the Milky Way at $\sim$14 kpc (Robin *et al.* 1992) some of the H I surveys extend into the halo of the galaxy. The interpretation of this data however would be would be difficult because of the uncertainties in the rotation curve and the gaseous velocity dispersion. For all the extra galactic systems, the flaring measurements do not extend beyond the optical disks. No information regarding the shape of the dark halo could be obtained.

Dissipationless galaxy formation simulations tend to produce triaxial DM halos (e.g., Frenk *et al.* 1988; Warren *et al.* 1992), with an intrinsic flattening distribution peaked at $q_\rho = c/a = 0.5$ ($\pm$ 0.15). Adding 10% baryonic matter (gas) and including gasdynamics to these simulations produces more oblate halos while q_ρ remains unchanged (Katz & Gunn 1991; Udry & Martinet 1994; Dubinski 1994). Observationally, all but the flattest shapes have been reported (for a summary, see Sec. 3.1.). Significantly flattened halos suggest that the process of galaxy formation is more dissipational, which might occur if a larger fraction of the initial density perturbation is baryonic. Since the flaring can be determined at lower inclinations as well, possibly at inclinations as low as 60$^{\rm o}$, the shape of dark matter halos surrounding many galaxies of different Hubble types can be determined. It will then be possible to gauge the significance of the highly flattened dark halo of NGC 4244, and place more stringent constraints on the process of galaxy formation.

Rich clusters contain $\sim 10h^{-1.5}$ % (by mass) hot X-ray emitting gas (Briel *et al.* 1992; Mushotzky *et al.* 1995, and references therein), with h the normalized Hubble constant (h=H$_0$/(100 km s^{-1}Mpc^{-1})). It might thus be useful to explore the process of galaxy formation over a larger range of baryon fractions. With a total mass-to-light ratio of 200 - 300 h (Bahcall *et al.* 1995) for these rich clusters, the mass-to-light ratio of cluster baryons ($M/\mathcal{L}_{\rm Bar,cl}$) equals 20 - 30 $h^{-0.5}$. Standard Big Bang nucleosynthesis (BBN) models (e.g., Walker *et al.* 1991) limits $M/\mathcal{L}_{\rm Bar,BBN}$ to the range 12 - 19 h^{-1}. From these limits it follows that for $h \geq 0.4$ essentially all baryons in the universe are located in rich clusters. In the region where the cluster and BBN estimates overlap ($0.2 \leq h \leq 0.8$), $M/\mathcal{L}_{\rm Bar} \sim 20h^{-0.74} \pm 7$. The dynamical mass-to-light ratios of individual galaxies (Broeils 1992, 1995) range from 4 to 100 h, with 80% of the systems between 6 and 20 h. It is thus possible that the dark halos of individual galaxies consist mainly of non-baryonic dark matter, but a 100% baryonic dark halo is also possible (Gott *et al.* 1974; Bahcall 1995; Sackett 1995). It is not clear however where, and in what form, these baryons reside in the galactic halos since all plausible forms of baryonic dark matter seem to be excluded (Hegyi & Olive 1986).

Pfenniger *et al.* (1994) reviewed cold, rotationally supported, molecular hydrogen as a dark matter candidate. In their model, small high density molecular "clumpuscules" form the building blocks of a highly clumped interstellar stellar medium (ISM) in which star formation is suppressed as a result of frequent collisions between the clumpuscules. Their model is best developed in the region beyond the optical disk. Inside the optical disk the state of the ISM is much more complex as a result of increased radiation field and metalicity. With the surface brightness of the background radiation equal to $\sim 8.5\ L_\odot\,{\rm pc}^{-2}$, the transition between the two regimes is expected to occur around $R \sim D_{25}/2$. The fact that in many galaxies the shape of the rotation curve due to the gas is similar to the observed rotation curve (Bosma 1981; Carignan *et al.* 1990; Carignan & Puche 1990; Broeils 1992, Chap. 10;

and see also Fig. 28) could then be explained if 3 - 10% of the gaseous surface density is in atomic form. Such might be expected in the context of clumpuscules hypothesis.

Since the self-gravity of the gas layer beyond the optical disk strongly affects the flaring[28] (Figure 8), I investigate whether the clumpuscules hypothesis is consistent with the flaring data presented in this paper. The pronounced features in the rotation curve due to the gaseous disk indicate that dark-to-gas surface density ratio varies with radius. Penny Sackett kindly provided the surface density distribution inferred from NGC 4244's rotation curve using a Keplerian as well as a flat extrapolation beyond the last measured point ($\Sigma_{\rm Kep}$ and $\Sigma_{\rm flt}$; see also Sackett 1995). Subtracting the stellar and gaseous surface densities yields the dark matter surface density distributions. Beyond 5 kpc ($\sim 2.5\ h_{\rm R}\sim D_{25}/2$) the inferred DM surface density is almost independent of the disk-halo decomposition, but is affected by the way the rotation curve is extrapolated: $\Sigma_{\rm DM,Kep} \approx 86 \exp{(-R/5.2)}$ (for $R \geq 5$ kpc), and $\Sigma_{\rm DM,flt} \approx 55 \exp{(-R/11.4)}\ M_\odot\,{\rm pc}^{-2}$(for $R \geq 5$ kpc). Almost independent of the stellar mass-to-light ratio. As mentioned above, the dark-to-H I surface density is not constant in NGC 4244, but instead rises in exponential fashion (with scale length $\sim 1.7 \pm 0.2$ kpc) from ~ 10 at the edge of the optical disk till ~ 100 the edge of the H I disk. This increase in dark-to-H I ratio is a result of the rapidly declining H I surface densities below column densities of $\sim 10^{20}$ cm^{-2}. Carignan & Puche (1990) find a similar effect for NGC 7793: for H I column densities below $5 10^{20}$ cm^{-2}, $\Sigma_{DM}/\Sigma_{\rm H\ I}$ increases exponentially. This contrasts Bosma's (1981) finding that, for column densities above $\sim 10^{20}$ cm^{-2}, the dark-to-H I surface density ratio is approximately constant[29]. To calculate the thickness of the H I layer in the presence of such a DM distribution, I assume that the clumpuscule disk is self-gravitating and isothermal with a velocity dispersion such that the thickness of the H I layer is as observed. I find dark matter velocity dispersions which are 1.1 and 1.3 times larger than $\sigma_{\rm H\ I}$, for $\Sigma_{\rm DM,Kep}$ and $\Sigma_{\rm DM,flt}$, respectively.

As the velocity dispersion in a clumpuscule-like ISM is not constant but depends on the scale on which it is measured (Pfenniger & Combes 1994), the velocity dispersion of the dark disk inferred above neither confirms nor falsifies the clumpuscule hypothesis. Since the interstellar radiation field decreases with distance it is not clear whether the strong radial variation of the dark-to-gas ratio is compatible with the clumpuscule hypothesis.

In accordance with van der Kruit's (1981) finding that the dark halo of NGC 891 can not be as flattened as the stellar distribution, the axial ratio of NGC 4244's halo (5:1) is smaller than the axial ratio of stellar disk (by a factor of $\sim$2 or $\sim$1.4 depending on whether the vertically distribution is exponential or sech^2). It seems that the "conspiracy of shapes"

[28]For NGC 4244, with its large fractional gas mass, the gaseous self-gravity is rather important.

[29]Note that the dark halo surface densities were calculated in three different ways: Sackett inverts an extrapolated rotation curve, Bosma uses Nordsieck's (1973) approximation to invert the rotation curve, while Carignan & Puche calculate the DM surface density from their best fit isothermal DM-halo model.

(Sackett *et al.* 1994), i.e. the similarity of the shapes of the dark and light distributions, breaks down for the flattest systems. Again, more determinations of the shape of dark halos will make it possible to gauge the frequency of highly flattened halos like the one of NGC 4244.

The ill-determined stellar mass-to-light ratio is the reason for the ambiguous determination of the radial density distribution of dark matter, as mentioned in Sec. 3.1.. One trend which is reasonably well established is that in the outer parts the rotation curves of high mass, intermediate mass, and low mass systems fall, remain flat, and increase, respectively (Casertano & van Gorkom 1992; Broeils 1992, Chap. 10; Persic *et al.* 1995). NGC 4244 does not fit in this general trend: its peak rotation velocity is low, while it decreases significantly beyond the optical disk: the rotation curve of NGC 4244 is more like the rotation curve of a more massive spiral. In fact, NGC 4244 falls exactly on the rotation-curve slope versus central surface brightness relation valid for fast ($\geq$ 180 km s^{-1}) rotators (Casertano & van Gorkom, 1991, their Fig. 8). With its low central surface brightness and rotation curve shape, NGC 4244 resembles more a scaled down bright galaxy than a scaled up dwarf. One other galaxy is known to have a low amplitude rotation curve with a significant decline beyond the optical disk, NGC 7793 (Carrigan & Puche, 1990), while none of the galaxies in the sample studied by Persic *et al.* (1995) have a rotation curve like NGC 4244 (Persic, private communications).

3.9. CONCLUSIONS

The potential of the global mass distribution, the self-gravity of the gas included, is used to calculate flaring curves for a series of models with various stellar mass-to-light ratios and dark halo flattenings (Chapter 2). Comparing the observed flaring curve with the various model curves I find that the flaring measurements do not further constrain the stellar $M/\mathcal{L}$. The shape of the halo on the other hand is well determined. The dark matter halo of NGC 4244 is significantly flattened, q_ρ=$0.2^{+0.3}_{-0.1}$ (E9 - E5), albeit less so than the stellar disk. The uncertainty in the derived halo flattening is dominated by the uncertainty in the measured gaseous velocity dispersion (Sec. 3.7.1.). The assumption that the vertical velocity dispersion equals the measured tangential dispersion is the most important potential systematic error: the measured flaring curve is consistent with a round halo if the gaseous velocity dispersion ellipsoid is anisotropic. In that case the vertical dispersion of the gas is 50 - 70% of the measured tangential velocity dispersion.

The rotation curve of the almost edge-on galaxy NGC 4244, determined from high resolution H I spectra, rises slowly to about 100 km s^{-1}at 5 kpc, remains flat till the edge of the optical disk at 10 kpc and decreases in Keplerian manner till the last measured point at seven optical scale lengths (14 kpc). The shape of the rotation curve is consistent with a stellar mass-to-light ratio between 50 and 100% of the maximum-disk value.

I developed a new technique to determine inclination and flaring for H I rich galaxies seen at inclinations larger than about 60° . This method has been used to determine the flaring curve for NGC 4244.

I like to thank Jacqueline van Gorkom for many valuable suggestions to improve this paper, for guidance in image processing, for advice in bicycle racing, for support and encouragement, and for discussing many interesting aspects of extra galactic astronomy. I would like to thank NRAO and the Kapteyn Astronomical Institute, for their hospitality as well as for their excellent software support. It was a great pleasure to discuss galactic structure and many aspects H I observations of galactic disks with Michael Rupen. I thank Juan Uson for discussing various aspects of calibrating VLA data and providing us with the wonderful UV-editing tasks UVLIN and UVMLN. Piet van der Kruit helped me a lot by providing the B-band photometry. I also thank Penny Sackett and John Hibbard for the disk dark matter curve, and an unbiased reading of a previous version of this paper. This research has made use of the NASA/IPAC Extragalactic Database (NED) which is operated by the Jet Propulsion Laboratory, CALTECH, under contract with the National Aeronautics and Space Administration. This work was supported in part through an NFS grant (AST-90-23254 to J. van Gorkom) to Columbia University.

3.10. Appendix A: DETERMINING THE ROTATION CURVE AND VELOCITY DISPERSION OF AN EDGE-ON GALAXY

In a manner similar to the tangent-point method employed for the Milky Way (e.g., Burton & Gordon 1978; Celnik *et al.* 1979), the gaseous velocity dispersion and the circular velocity can be derived from the extreme velocity tails of spectra taken on the major-axis of an edge-on galaxy. In this section I investigate how gradients (along the line-of-sight) in surface density, rotation speed and velocity dispersion affect this derivation. Gradients perpendicular to the line-of-sight, beam smearing, are also addressed.

For a galaxy, in which all gas moves at exactly the circular velocity ($V_{\rm c}$), gas on the major axis moves at the local rotation velocity. Other positions have lower projected velocities, $V_{\rm p}$ [Eqn. (51)]. In reality, the velocity dispersion of the gas broadens the sharp cutoff at $V_{\rm c}(R)$ and moves the peak of maximum emission closer to the systemic velocity. The spectrum, $I(x,V,d;S)$, at a point[30] (x,d) on the sky depends on the surface density distribution of the gas, the distribution perpendicular to the plane, the gaseous velocity dispersion, the rotation curve, and the channel response function $S(V';V,\Delta V)$, defined by Eqn. (62). After summing the data along the minor axis, the dependence on minor axis position and the vertical distribution disappear so that the spectrum (or "XV plot") is given by:

$$I(x,V;S) \quad = \quad \frac{K}{\sqrt{2\pi}} \int dy \, \frac{\Sigma(y)}{\sigma(y)} \int dV' \; S(V';V,\Delta V) \; e^{\left(-\frac{1}{2}[(V'-V_{\rm P}(y))/\sigma(y)]^2\right)} \quad , \tag{59}$$

with and K a proportionality constant related to the choice of units, $y=\sqrt{R^2-x^2}$, and

$$V_{\rm p}(y) \quad = \quad V_{\rm c}(R) \times \frac{x}{\sqrt{x^2+y^2}} \quad \approx V_{\rm c}(x) + \frac{y^2}{2x^2}(ax - V_{\rm c}(x)) \quad . \tag{60}$$

Here $V_{\rm c}(R) \approx V_{\rm c}(x) + a\,(R-x)$, and a the gradient in the rotation curve (km s^{-1}/kpc). A point somewhere along the line of sight whose projected velocity is σ km s^{-1} lower than the rotation speed will hardly influence parts of the spectrum at velocities larger than $V_{\rm c}(x)$. Thus, the spatial integral in Eqn. (59) can be limited to a maximum, $\pm y_{\rm max}$ so that only gas "close" to the major axis will contribute significantly to the extreme velocity tails (EVTs). Eqn. (60) provides an estimate for $y_{\rm max}$:

$$y_{\rm max} \quad \approx \quad x \sqrt{-\frac{2\,\sigma(x)}{ax - V_{\rm c}(x)}} \quad . \tag{61}$$

For NGC 4244, typical values for $\epsilon_{\rm m}(= y_{\rm max}/x)$ decrease from 0.85 at 1 kpc to 0.33 at 12 kpc. The velocity dispersion and the surface density can be expanded around $R=x$ as well:

[30] The coordinate system is defined in Sec. 3.4.1..

$\sigma(y) \approx \sigma(x)\ \left(1 + \frac{1}{2}\, bx\epsilon^2\right)$, and $\Sigma(y) \approx \Sigma(x) + \frac{1}{2}\, cx\epsilon^2$, where b is the fractional gradient of the velocity dispersion (kpc^{-1}), and c the gradient in surface density ($M_\odot\,\mathrm{pc}^{-2}$/kpc).

For spectral line data obtained with the VLA which is not Hanning smoothed (as is the case for the observations presented in this paper), a channel of width ΔV, centered at V, is sensitive to emission at other velocities V' as well. The channel response function is given by (Rots 1990):

$$S(V'; V, \Delta V) \;=\; \frac{\sin\left(\pi(V'-V)/\Delta V\right)}{\pi(V'-V)/\Delta V}\ . \tag{62}$$

The strong sidelobes of S are reduced by more than an order of magnitude when integrated over the width of a channel (the 1^{st}, 2^{nd}, 3^{rd}, and 4^{th} channels have an effective sensitivity of 100%, +8.6%,-1.9%, and +0.83%, respectively). Limiting the velocity range (to $\pm\frac{1}{2}\Delta V$) of the second integral in Eqn. (59) and taking S to be unity allows for an analytic approximation of $I(x, V; S)$, which can then be used to gauge the importance of line-of-sight gradients of the variables.

Approximating the Gaussian term in Eqn. (59) by a parabola and integrating the spatial integral up to ϵ_{m}, the spectrum can be written as:

$$I(x,V) \;\approx\; \left(\frac{\epsilon_{\mathrm{m}}\ K\ \Delta V\ \Sigma}{\sqrt{2\pi}\sigma}\right)\ e^{-\frac{1}{2}\left(\frac{W}{\sigma}\right)^2} \times$$
$$\left\{2 \;-\; \frac{\epsilon_{\mathrm{m}}^2 W V_{\mathrm{c}}}{3\sigma^2} \;+\; \frac{x\epsilon_{\mathrm{m}}^2}{3}\left[\left(\frac{aW}{\sigma^2}\right) \;+\; b\left(\frac{W^2}{\sigma^2} - 1\right) \;+\; \frac{c}{\Sigma}\right]\right\}\ , \tag{63}$$

where all galaxian properties are evaluated at radius $R = x$, and with $W = V - V_{\mathrm{c}}(x)$. The multiplicative term in Eqn. (63) is a Gaussian function of dispersion σ. The first term within the curly brackets results from material on the major axis, the second term arrises due to material close to the major axis, while the last three terms originate due to radial gradients in rotation speed, dispersion and surface density, respectively. Except in the inner 6 kpc, where beam smearing is important as well, Eqn. 63 represents the measured EVTs well. A beam smearing correction could be obtained by from an approximation of the convolution of the spectrum (63) with the beam. However, as this leads to quite ugly equations, another approach is followed. As we have seen above, the EVTs of an XV plot contain information about the rotation curve and velocity dispersion. A Gaussian fit to such a EVT yield a value for the position and width of this Gaussian[31]. Line-of-sight and beam smearing effects

[31] In practice multiple components are fitted to the full spectrum such that the EVT is dominated by one component. Because of the additional components (more degrees of freedom) the errors are overestimated. The AIPS tasks SLICE and SLFIT were used to perform the Gaussian fits. However, the version of these tasks which are part of the standard AIPS release re-sample every slice to a 512 grid, as a result of which the calculated errors are meaningless. I therefore used special versions of SLICE and SLFIT which do not re-sample the data.

cause these values to deviate from the intrinsic rotation speed and velocity dispersion. The magnitude of these deviations can be empirically found by comparing the values obtained from fits to a simulated[32] XV plot with the parameters used in the calculation of the simulated XV plot. I find:

$$\sigma_{\rm gas} \approx \frac{\sigma_{\rm XV;10}}{(0.9 + \exp[-R/4])} \qquad R \leq 10{\rm kpc} \tag{64}$$

$$\sigma_{\rm gas} \approx \frac{\sigma_{\rm XV;38,55}}{(0.9\exp[-10/4] + \exp[(R-10)/17])} \qquad R > 10{\rm kpc} \tag{65}$$

The subscripts "10", "38", and "55" refer to the beamsize of the data set for which the correction is appropriate. The "XV" subscript refers to the value as fitted to the extreme velocity envelope of the XV plot. Note that the true gaseous velocity dispersion is always smaller than the dispersion of the extreme velocity envelope. As these corrections depend on the input parameters (e.g., beam smearing is insignificant for a flat rotation curve), the input parameters for the calculation of the simulated XV plot should be close to the intrinsic rotation and dispersion curves: this problem is solved by iterating several times. An estimate of $\sigma_{\rm XV}$ can also be obtained by counting the number ($N_{\rm 0,P}$) of velocity channels between the zero and peak emission level of the EVT. This estimate is calibrated by generating Gaussian distributions with a range of dispersions centered at various locations within a velocity channel: ($\sigma_{\rm XV} = (2.4N_{\rm 0,P} - 0.6 \pm 1) \times \frac{\Delta V_{\rm chan}}{5.2}$). Since $N_{\rm 0,P}$ as determined from the data is generally equal to the value determined from the simulated XV plot, I conclude that the velocity dispersion (and rotation curve, see below) as determined from the Gaussian-fit method is reliable.

Because these relations depend on beam size, channel width, surface density distribution, and the rotation curve, these relations are specific to the observations of NGC 4244 presented in this paper. The errors, 3σ, about 20% and 5% in the inner and outer part of the galaxy, are largest in those regions with strong surface density gradients.

The corrections required to determine the rotation curve from the XV-plots are given by:

$$V_{\rm rot;10}\ (R) \approx V_{\rm XV;10} + (1.3 \times \exp[-R/4.0] + 0.35) \times \sigma_{\rm XV;10} \tag{66}$$

$$V_{\rm rot;38,55}(R) \approx V_{XV;38,55} + (1.0 \times \exp[-R/4.0] + 0.35) \times \sigma_{\rm XV;38,55}\ . \tag{67}$$

In regions where the surface density changes rapidly, the smearing correction is least reliable: differences between input and output rotation curves of order 3 - 5 km s^{-1} occur in the inner 5 kpc of the simulated XV plots.

[32]Using the procedure outlined in Appendix 3.11..

These correction are then applied to the fitted rotation and dispersion values obtained from the data. The resulting dispersion and rotation curves are shown in Figs. 22 and 23, respectively. At some locations, the data EVTs are very different from the simulated EVTs, while adjacent positions have similar EVTs: these locations are likely to be affected by local irregularities and have been discarded.

Because beam smearing effects are not important beyond 6 kpc, Eqn. (63) can be used to investigate the dependence of the shape of the EVTs on gradients in $V_{\rm c}(R)$, $\Sigma(R)$, and $\sigma(R)$. Since for a given range in y, or $\epsilon_{\rm m}$, only a small range in R is sampled so that gradients in the rotation curve are unimportant. Gradients along the line of sight in surface density and dispersion cause changes in $V_{\rm XV}$ and $\sigma_{\rm XV}$ (in km s^{-1}, where the subscripts refer to the values as derived from the XV plot):

$$\Delta V_{\rm XV} \approx (-3 \pm 0.7)\, b \;, \tag{68}$$

$$\Delta \sigma_{\rm XV} \approx (1.8 \pm 0.8)\, b + (0.84 \pm 0.12) \left(\frac{c}{\Sigma}\right) \qquad (c \leq 0) \;, \tag{69}$$

while the c-dependence in (69) is absent for $c > 0$. Beyond the optical disk, typical values for c/Σ and b are -0.5 and 0.05, respectively. The smearing corrections [Eqns. (64) through (67)] take these gradients into account. From Eqn. (69) it follows that in order to *over* estimate $\sigma_{\rm XV}$ (and hence σ) large *positive* line of sight gradients in the dispersion are required. With $\sigma_{\rm XV}$ of the order of 10 km s^{-1}, a 10% over estimate is possible if the dispersion along the line of sight increases to 15 km s^{-1} over a distance of 1 kpc. If such a strong σ-gradient would exist in the radial direction as well, it would certainly be noticed.

3.11. APPENDIX-B: SIMULATING VLA SPECTRAL LINE OBSERVATIONS

In order to facilitate the interpretation of H I spectral line data I developed software which simulates VLA H I observations of galaxies. The accuracy of the determination of rotation and velocity dispersion curves from XV plots, the beam-smearing corrections, the thickness-and-inclination determination method, can all be gauged by comparing the "observations" of such a simulated galaxy with the input parameters. Input parameters to this program (VLASIM) are: the observing geometry, $\Sigma(R)$, $V_{\rm rot}(R)$, and $\sigma_{\rm gas}$. The vertical density distribution of the gas layer is calculated employing a physical model for the potential of the galaxy (the multi-component method, Chapter 2) which yields the gaseous volume density. The rotation speed is assumed[33] to be constant with height above the plane. VLASIM then integrates the amount of hydrogen along lines of sight from the observer through the galaxy, and distributes this amount over the appropriate channels. When the line of sight integrations are done, the spectral line cube is smoothed to the requested resolution followed by the addition of realistic noise (if so desired).

[33]For several disk-halo models, rotation curves at different z-heights were calculated, all showing that the rotation speed does not vary significantly ($\leq$ 5 km s^{-1}) in the region where gas is found ($\mid z \mid \leq 3FWHM_{\rm z,gas}$).

3.12. APPENDIX-C: THE EFFECTS OF KINEMATICAL DISTORTIONS

As discussed in Sec. 3.5., knowledge of the rotation curve allows us to determine the intrinsic thickness of the gas layer. However, the method is sensitive to deviations from the assumed rotation curve. Spiral arm streaming motions of several tens of percent of the rotation speed (several tens km s^{-1}), are not uncommon in spiral galaxies (e.g., Visser 1980; Vogel *et al.* 1988; Tilanus & Allen, 1993; Boulanger & Viallefond, 1992), so that locally the velocity deviates from the circular velocity. When a line of sight is along a spiral arm, there will be a net shift in the radial velocity (type 1), when the line of sight crosses a spiral arm, the radial velocity will not be affected but the dispersion will be larger[34] (type 2). In this section I determine which parts of the galaxy are most susceptible to non-circular motions and present a weighting scheme which minimizes the effects of non-circular motions: a summary is presented in the next section (3.12.1.).

The galactocentric coordinates [(x, y, z) or (R, θ, z)] are related to the celestial coordinates [(x,d) centered on the galaxy) in the following way:

$$x = R\cos\theta \ , \tag{70}$$

$$d = R\cos i \sin\theta + z\sin i \ . \tag{71}$$

where the position angle of the major axis was taken east-west (90$^{\rm o}$) and where z is the height above the plane. If gas located at $(R, \theta, 0)$ has a line of sight streaming velocity of

$$\Delta V = \sin i \left[V_{\rm rot}(R_0)\cos\theta_0 - V_{\rm rot}(R)\cos\left(\theta_0 + \Delta\theta\right)\right]$$

with respect to a position $(R_0, \theta_0, 0)$, this position will be "seen" in the same channel as $(R_0, \theta_0, 0)$ is. Similarly, a channel ΔV km s^{-1} wide "sees" gas in an area delimited by θ_0 and θ. Expanding $\cos\left(\theta_0 + \Delta\theta\right)$ to second order around θ_0, and assuming that rotation curve around R_0 is constant, I approximate the above equation and solve for $\Delta\theta$.

$$\Delta V \approx V_{\rm rot}(R_0)\sin i \left[\sin\theta_0 \ \Delta\theta + \frac{1}{2}\cos\theta_0(\Delta\theta)^2\right] \quad \text{, and} \tag{72}$$

$$\Delta\theta = \tan\theta_0 \left[-1 + \sqrt{1 + \frac{2\Delta V}{V_{\rm rot}(R_0)\sin i}\frac{\cos\theta_0}{\sin^2\theta_0}}\ \right] \ . \tag{73}$$

The requirement that the two points [$(R_0, \theta_0, 0)$ and $(R, \theta, 0)$] have the same major axis distance (r) leads [via Eqn. (70)] to the following relation for ΔR ($\equiv R - R_0$):

$$\frac{\Delta R}{R_0} \approx \tan\theta_0 \left(\frac{\Delta\theta}{1 - \tan\theta_0 \ \Delta\theta}\right) \tag{74}$$

In the lower panel of Figure 32 I present the relations, both practically independent of inclination, for $\Delta\theta$ and ΔR graphically for the case where ΔV = 10 km s^{-1} and

[34] I thank Ron Allen for pointing this out to me.

$V_{\rm rot}(R_0) = 100$ km s^{-1}. Although this galaxy model is extremely simple, the opening angles as determined for a more realistic model behave similarly: the high velocity channels (small θ_0) are wider than the low velocity channels. The fractional range in galactocentric radius is small so that the approximate relation for ΔV (72) is reasonable, whether or not the rotation curve is constant around R_0.

If the positions (R_0, θ_0, z_0) and $(R, \theta, 0)$ project on the same position on sky, and if due to a streaming motion they also have the same velocity, then their positions in the observer's spectral-line cube will be the same. The equivalent vertical height of this streaming motion (or, equivalently, a channel ΔV km s^{-1} wide) equals z_0:

$$z_0 \approx R_0 \left(\frac{\Delta\theta}{\cos\theta_0 \tan i} \right) . \tag{75}$$

I plotted the projection of z_0 ($\equiv z_0 \sin i$) in the one but lowest panel of Figure 32. The curves are labeled with the corresponding galactocentric radii. For $i = 85°$ its value is small compared to the projected vertical thickness of the gas layer, but its importance relative to the projected vertical thickness of the gas layer grows rapidly with decreasing inclination ($\propto \tan^{-1} i$).

The systematic errors introduced by streaming motions are more easily understood when considering the corresponding planar width of the CSDD:

$$\begin{aligned} \Delta Y(\Delta V) &\approx R_0 \left(\frac{\Delta\theta}{\cos\theta_0} \right) \\ &\approx R_0 \left[\cos\theta_0 \left(1.81 \left(\frac{V_{\rm rot}(R_0)\ \sin i}{2\Delta V} \right) \sin^{1.2}\theta_0 + \sqrt{\frac{V_{\rm rot}(R_0)\ \sin i}{2\Delta V} \cos\theta_0} \right) \right]^{-1} . \end{aligned} \tag{76}$$

In the region close to the major axis, kinematical distortions have an effect proportional to the square root of the fractional velocity deviation (2^{nd} term), in the lower velocity channels the proportionality is approximately linear (1^{st} term). Thus, the channels close to the major and minor axes have long pathlengths through the galactic disk and are hence easily affected by kinematical or surface brightness irregularities (Fig. 32, third panel from below).

Streaming motions of type 1 cause the centers of the CSDD to shift along the line of sight, typically by $\pm\Delta Y$ [see also Eqn. (78)]. In the almost edge-on situation, the two sides of the CSDD are overlapping so that the projected planar width [Eqn. (53)] and its error are dominated by the $Y_{\rm C}$ term. Visser (1980) presents model velocity fields for M 81 which include spiral arm streaming motions (his Fig. 10). The equivalent CSDD map (with 20 km s^{-1} wide channels) results after deprojection. From these velocity fields it is clear that the centers of the CSDDs are shifted substantially: outwards on the outside of the arm and inwards on the inside of the arm. The strong kinks follow the spiral arm and would produce sudden changes in the separation of the sides of the CSDDs and in the width thereof, over a large range in azimuth. If streaming motions are present, but the resulting CSDD-kinks are not taken into account in the analysis, the inferred widths may show strong gradients when crossing a spiral arm. Such may be the reason for the large thickness gradients seen in NGC 891 (Rupen 1991a) and NGC 4244 (Sec. 3.7.1.).

At lower inclinations, when the two sides of the CSDD are separated, streaming motions of type 2 affect the width determination [Eqn. (79)], while the errors on Y (type 1 streaming motions) hamper the determination [via Eqn. (55)] of the inclination. This is illustrated in the top panel of Figure 32, where I plot the inclination error resulting from a velocity shift of 10 km s^{-1}:

$$\Delta i \approx \frac{\cos i}{\sin^2 i} \frac{\Delta\theta}{\sin\theta_0 \cos\theta_0} \quad . \tag{77}$$

Small streaming motions occurring close to either the minor or the major axis can cause large errors in the inferred inclination. Furthermore, the inclination errors are strongly inclination dependent: $\Delta i(i = 65^{\mathrm{o}}) \approx 6\Delta i(i = 85^{\mathrm{o}})$.

3.12.1. Summary

I will use the above determined systematic errors estimates in the thickness & inclination determination process. The effect of spiral arm streaming motions is to either shift the center of the CSDD along the line of sight or to increase the apparent velocity dispersion, the former having more severe effects. To our advantage, the expected systematic errors scale with the width of a CSDD wing (calculated for a given gaseous velocity dispersion σ_{gas}),

$$\delta Y_{\mathrm{C}} \approx \frac{\Delta Y(\Delta V)}{\Delta Y(\sigma_{\mathrm{gas}})} \times FWHM_{\mathrm{C}}(\sigma_{\mathrm{gas}}) \ , \tag{78}$$

and

$$\delta FWHM_{\mathrm{C}}(\sigma_{\mathrm{gas}}) \approx \left(\sqrt{1 + \left(\frac{\Delta Y(\Delta V)}{\Delta Y(\sigma_{\mathrm{gas}})} \right)^2} - 1 \right) \times FWHM_{\mathrm{C}}(\sigma_{\mathrm{gas}}) \ , \tag{79}$$

are easily calculated from the CSDD model and Eqn. (76). These systematic errors increase towards lower inclinations and are proportional to $(\sin i \ \sin\theta\cos\theta)^{-1}$: the area around both principal axes are most easily affected by streaming motions.

3.13. APPENDIX-D: OPTICAL DEPTH EFFECTS

In the Milky Way the optical depth in the H I line is substantial within a few degrees from the galactic plane (e.g., Dickey *et al.* 1983). Typically, the total emission along the line of sight is under estimated by 15%. Similar values are found for edge-on external systems (Haynes & Giovanelli 1984). We thus expect similar values for NGC 4244. Braun & Walterbos (1992) estimate that the cold interstellar medium, which is mostly responsible for the absorption (see below), has a volume filling factor of about 1 - 8%, for the Milky

Way and M31, respectively. This cold material forms a layer two to three times thinner than the warm H I (e.g., Kulkarni & Heiles 1988; Braun & Walterbos 1992). For NGC 4244, we thus expect that emission profiles perpendicular to the major axis might be affected by absorption on the midplane, resulting in larger apparent widths. However, from the peak surface brightness and apparent width measurements (Fig. 26) such effects are not obvious: profiles with a high peak column density do not seem to be broader. A more detailed, albeit idealized, calculation of the optical depth is given below.

The optical depth in the H I line for a uniform medium of length l and number density n is given by Braun & Walterbos. Their Eqn. (7) reads:

$$\tau \quad = \quad 170 \frac{n\, l}{T_{\mathrm{s},100}\, \Delta V} \quad , \tag{80}$$

with $T_{\mathrm{s},100}$ the spin temperature in units of 100 K, and ΔV the width of the channel. In Sec. 3.4. the surface density, the rotation curve and the velocity dispersion were derived assuming low optical depth. Those derived quantities can be used to evaluate the quantities in Eqn. (80) and check the validity of the assumption of low optical depth. The CSDD maps provide the H I surface density for which the projected velocity equals the observing velocity ($\pm\frac{1}{2}\Delta V$). Investigating these CSDD channel maps (Fig. 24) we find typical peak column densities of 0.5 - 1 $M_\odot\,\mathrm{pc}^{-2}$ for galactocentric radii smaller than 7 kpc, and much less beyond. In edge-on geometry, the surface density distribution along the line of sight is a double Gaussian [Eqn. (52)] with a typical width ($FWHM_\mathrm{p}$) for each component of 3 $\pm$ 1 kpc. The H I volume number density is given by: $n = 5.5\ 10^{-3}\,(\Sigma_1/FWHM_{\mathrm{z},1})\ \mathrm{cm}^{-3}$), where the units are $M_\odot\,\mathrm{pc}^{-2}$ and kpc. The optical depth can then be rewritten as:

$$\tau \quad = \quad 0.156 \frac{\Sigma_1\, FWHM_{\mathrm{p},3}}{FWHM_{\mathrm{z},1}\, T_{\mathrm{s},100}} \quad , \tag{81}$$

where a channel width of 6.2 km s^{-1} was used. Typical values for the spin temperature of the cold component of the interstellar medium range from 100 - 175 K (for the Milky Way and M31, respectively; Braun & Walterbos 1992). Smaller values are found in individual clouds (Spitzer 1978, p. 48, and references therein). Taking the model widths as representative for the thickness of the gas layer ($\sim$ 250 pc), and assuming that the cold medium fills the entire volume we find $\tau \sim 0.33$ (30% attenuation). If the cold medium is clumpy with a low filling factor, like in the Milky Way, we might expect 3 clouds per kpc with an optical depth $\geq$ 1 (Kulkarni & Heiles 1988). In exactly edge-on geometry this would correspond to a large optical depth indeed. However, at an inclination of 85° the path through the galaxy ($\sim$ 3 kpc) corresponds to a change in z of $\sim$ 260 pc (about three times the thickness of the cold gas layer), so that the number of absorbing clouds per line of sight is reduced. Because the pathlengths $FWHM_\mathrm{p}$ are comparable for all velocity channels, the optical depth effects are comparable in all channels (in the inner 7 kpc).

Beyond 7 kpc the surface densities are much smaller so that optical depth effects are not important in the derivation of the shape of the DM halo.

REFERENCES

Aaronson, M., Bothum, G., Mould, J. R., 1986, ApJ, 302, 536

Albada, T.S., van, Bahcall, J.N., Begeman, K., Sancisi, R., 1985, ApJ, 295, 305

Albada, T.S., van, Sancisi, R., 1986, Phil. Trans. R. Soc. Lond. A., 320, 447

Amendt, P., Cuddeford, P., 1994, ApJ, 435, 93

Athanassoula, E, Bosma A., Papaioannou, P., 1987, A&A, 179, 23

Bahcall, N.A., 1995, in Dark Matter, edited by S.S. Holt, C.L. Bennet (AIP conference proceedings 336), p. 201

Bahcall, N.A., Lubin, M.L., Dorman, V., 1995, ApJ, 447, L81

Barteldrees, A., Dettmar, R. J., 1994, A&AS, 103, 475

Bergstrom, J., Gehrz, R.D., and Jones, T.J., 1992, PASP, 104, 695

Bicay, M.D., Helou, G., 1990, ApJ, 362, 59

Binney, J. ,Tremaine, S. , 1987, Galactic Dynamics, Princeton University Press

Binney J., Mamon G.A., 1982, MNRAS, 200, 361

Binney J., May, A., Ostriker, J.P., 1987b, MNRAS, 226,149

Blitz, L., Magnani, K., Mundy, L., 1984, ApJ, 282, L9

Bosma, A., 1981, AJ, 86, 1971

Botinelli, L., Gouguenheim, Fouqué, P., Paturel, G., 1990 A&AS, 82, 391

Bottema, R, 1993, A&A, 275, 16

Bottema, R, 1989, A&A, 221, 249

Bottema, R, 1988, A&A, 197, 105

Boulanger, F, Viallefond, F., 1992, A&A, 266, 37

Braun, R., 1995, A&AS, 114, 409

Braun, R., 1991, ApJ, 372, 54

Braun, R., Walterbos, R.A.M., 1992, ApJ, 386,120

Bregman, J.N., Glassgold, A.E., 1982, ApJ, 263, 564

Briel, U.G., Henry, J.P., Boehringer, H., 1992, A&A, 259, L31

Broeils, A.H., 1995, in in Dark Matter, edited by S.S. Holt, C.L. Bennet (AIP conference proceedings 336), p. 125

Broeils, A.H., 1992, Ph. D. Thesis, Rijksuniversiteit Groningen

Burkert, A., Truran, J.W., Hensler, G., 1992, ApJ, 391, 651

Burstein, D., Heiles, C., 1984, ApJS, 54, 33

Burton, B.W., Gordon, M.A., 1978, A&A, 63, 7

Carignan, C., Charbonneau, P., Boulanger, F., Viallefond, F., 1990, A&A, 234, 43

Carignan, C., Puche, D., 1990, AJ, 100, 394,

Casertano, S., 1983, MNRAS, 203, 735

Casertano, S., van Gorkom, J. H., 1991, AJ, 101, 1231

Celnik, W., Rohlfs, K., Braunsfurth, E., 1979, A&A, 76, 24

Condon, J.J., 1987, ApJS, 65, 485

Corbelli, E., Schneider, S. E., Salpeter, E. E., 1989, AJ, 97, 390

Deharveng, J.M., Bixler, J., Joubert, M., Bowyer, S., Malina, R., 1986, A&A, 154, 119 de Vaucouleurs, G., 1975, in Stars and Stellar Systems, edited by A. Sandage, M. Sandage, J. Kristian (Chicago Univ. Press), Chapter 14, p 557

de Vaucouleurs, G., de Vaucouleurs, A., Corwin, H.G., 1976, Second Reference Catalogue of Bright Galaxies, Austin, University of Texas Press (RC2)

Dickey, J.M., Hanson, M.M, Helou, G., 1990, ApJ, 352, 522

Dickey, J.M., Kulkarni, S.R., van Gorkom, J.H., Heiles, C.E., 1983, ApJS, 53, 591

Dokkum, P.G. van, Peletier, R.F., Grijs R. de, Balcells M., 1994, A&A, 286, 415

Dubinski, J., 1994, ApJ, 431, 617

Efstathiou, G, Lake, G., Negroponte, J, 1982, MNRAS, 199, 1069

Frenk, C. S., White, S.D.M., Davis, M., Efstathiou, G., 1988, ApJ, 327, 507

Gilmore G., 1990, in The Milky Way as a Galaxy, edited by R. Buser, I.R. King (University Science Books), p. 350

van Gorkom, J.H., 1993, in The Environment and Evolution of Galaxies, 1993, edited by D. Hollenbach, H. Thronson (Kluwer, Dordrecht/Boston/London), p. 345

Gott, J.R., III, Gun, J.E., Schramm, D.N., Tinsley, B.M., 1974, ApJ, 194, 543

Haynes, M. P., Giovanelli, R., 1984, AJ, 89, 758

Hegyi, D., Olive, K.A., 1986, ApJ, 303, 56

Hoffner, P., Sparke, L., 1994, ApJ428, 466

Huchtmeier, W.K., 1975, A&A, 45, 259

Huchtmeier,W.K., Seiradakis, J.H., 1985, A&A, 143, 216

Hummel, E., Sancisi, R., Ekers, R.D., 1984, A&A, 133, 1

Irwin, J. A., Seaquist, E.R, 1991, ApJ, 371, 111

Jong, R.S. de, 1995, Ph.D. Thesis, Rijksuniversiteit Groningen

Jong, R.S. de, Kruit, P.C. van der, 1994, 1994, A&AS, 106, 451

Kamphuis, J., 1993, Ph.D. Thesis, Rijksuniversiteit Groningen

Katz, N., Gunn, J.E., 1991, ApJ, 377, 365

Knapp, G.R., 1987, PASP, 99, 1134

Kraan-Korteweg, R.C., Tammann, G.A., 1979, Astron. Nachr., 300, 181

Kruit, P.C. van der, 1988, A&A, 192, 117

Kruit, P.C. van der, 1981, A&A, 99, 298

Kruit, P.C. van der, Searle, L., 1981a, A&A, 95,105

Kruit, P.C. van der, Searle, L., 1981b, A&A, 95,116

Kruit, P.C. van der, Searle, L., 1982a, A&A, 110, 61

Kruit, P.C. van der, Searle, L., 1982b, A&A, 110, 79

Kruit, P.C. van der, Shostak, G.S., 1982, A&A, 105, 351

Kulkarni, S.R., Heiles, C., 1988, in Galactic and Extragalactic Radio Astronomy, edited by G.L. Verschuur and K.I. Kellermann (Springer-Verlag), Chapter 3

Kulkarni, S.R., Blitz, L., Heiles, C., 1982, ApJ, 259, L63

Lake, G., Feinswog, L., 1989, AJ, 98,166

Larson, R.B., Tinsley, B.M., 1978, ApJ, 219, 46

Malhotra, S., 1994, ApJ, 433, 687

Malhotra, S., 1995, ApJ, 448, 138

Maloney, P., 1993, ApJ,414, 41

Marel, R. P., van der, 1991, MNRAS, 248, 515

Martinet, L., 1988, A&A, 206, 253

Merrifield, M.R., 1992, AJ, 103, 1552

Mushotzky, R.F., Loewenstein, M., Arnaud, K., Fukazawa, Y, 1995, in in Dark Matter, edited by S.S. Holt, C.L. Bennet (AIP conference proceedings 336), p. 231

Napier, P.J., Thompson, A. R, Ekers, R. D., 1983, 71, 1295 IEEE Proceedings

Nordsieck, K.H., 1973, ApJ, 184, 719

Olling, R.P., 1995, AJ, 110, 591, (Paper I;Chapter 2)

Olling, R.P., 1995b, Ph.D. Thesis, Columbia University (in preparation)

Olling, R.P., van Gorkom, J.H., 1995, in Dark Matter, edited by S.S. Holt, C.L. Bennet (AIP conference proceedings 336), p. 121

Parker, E.N., 1966, ApJ, 145, 811

Peletier, R.F., Valentijn, E.A., Moorwood, A.F.M, Freudling, W., 1994, A&AS, 108, 621

Persic, M., Salucci, P., Stel, F., 1995, submitted to MNRAS, astro-ph/9506004

Pfenniger, D., Combes, F., Martinet, L., 1994, A&A, 285, 79

Pfenniger, D., Combes, F., 1994, A&A, 285, 94

Rice, W., 1993, AJ, 105, 67

Rix, H.W., Zaritsky, D., 1995, to appear in ApJ, astroph-950156

Robin, A., C., Crézé, M., Mohan, V, 1992, ApJ, 400, L35

Rots, A., 1980, A short guide for spectral line observers

Rubin, V.C., Burnstein, D., Ford, W.K., Thonnard, N., 1985, ApJ, 289,81

Rupen, M.P., 1991a, Ph.D. Thesis, Princeton University

Rupen, M.P., 1991b, AJ, 102, 48

Sackett, P.D., 1995, To appear in, Techniques, Puzzles and Implications for Lensing, edited by C. Kochanek, J. Hewitt (Proc. IAU Symp. 173, Melbourne) ; astro-ph/950898

Sackett, P.D., Pogge R.W., 1995 in Dark Matter, edited by S.S. Holt, C.L. Bennet (AIP conference proceedings 336), p. 141

Sackett, P.D., Rix, H.W., Jarvis, B.J., Freeman, K,C., 1994, ApJ, 436, 629

Sackett, P.D., Sparke, L.S., 1990, ApJ, 361, 408

Sage, L.J., 1993, A&A, 272, 123

Sandage, A., Bedke, J., 1994, in The Carnegie Atlas of Galaxies (Carnegie Institution of Washington)

Sandage, A, Tammann, G.A., 1975, ApJ, 196, 313

Sancisi, R., Allen, R.J., 1979, A&A, 74, 73

Schwarzschild, M., AJ, 59, 273

Schlickeiser, R., Werner, W., Wiebelinski, R., 1984, A&A, 140, 277

Sommer-Larsen, J., Zhen, C., 1990, MNRAS, 242, 10

Spitzer, L., Jr., Physical Processes in the Interstellar Medium (New York, John Wiley and Sons)

Steiman-Cameron, T.Y., Kormendy, J., Durisen, R.H., 1992, AJ, 104, 1339

Terndrup, D.M., Davies, R.L., Frogel, J.A., DePoy, D.L., Wells, L.A., 1994, ApJ, 432, 518

Tilanus, R.P.J., Allen, R.J., 1993, A&A, 274, 707

Tinsley, B. M., 1981, MNRAS, 194, 63

Udry, S., Martinet, L., 1994, A&A, 281, 314

Visser, H.C.D., 1980, A&A, 88, 159

Vogel, S.N., Weymann, R., Rauch, M., Hamilton, T., 1995, ApJ, 441, 162

Vogel, S.N., Kulkarni, S.R., Scoville, N.Z., 1988, Nature, 334, 402

Wainscoat, R.J., Freeman, K.C., Hyland, A.R., 1989, ApJ, 337, 163

Walker, T.P., Steigman, G., Schramm, D.M., Olive, K.A., Kang, H., 1991, ApJ, 376, 51

Warmels, R.H., 1988, A&AS, 72

Warren, M.S., Quinn, P.J., Salmon, J.K., Zurek, W.H., 1992, ApJ, 399, 405

Worthey, G., 1994, ApJS, 95, 107

Wouterloot, J.G.A., Brand, J., Burton, W.B.., Kwee, K.K., 1990, A&A, 230, 21

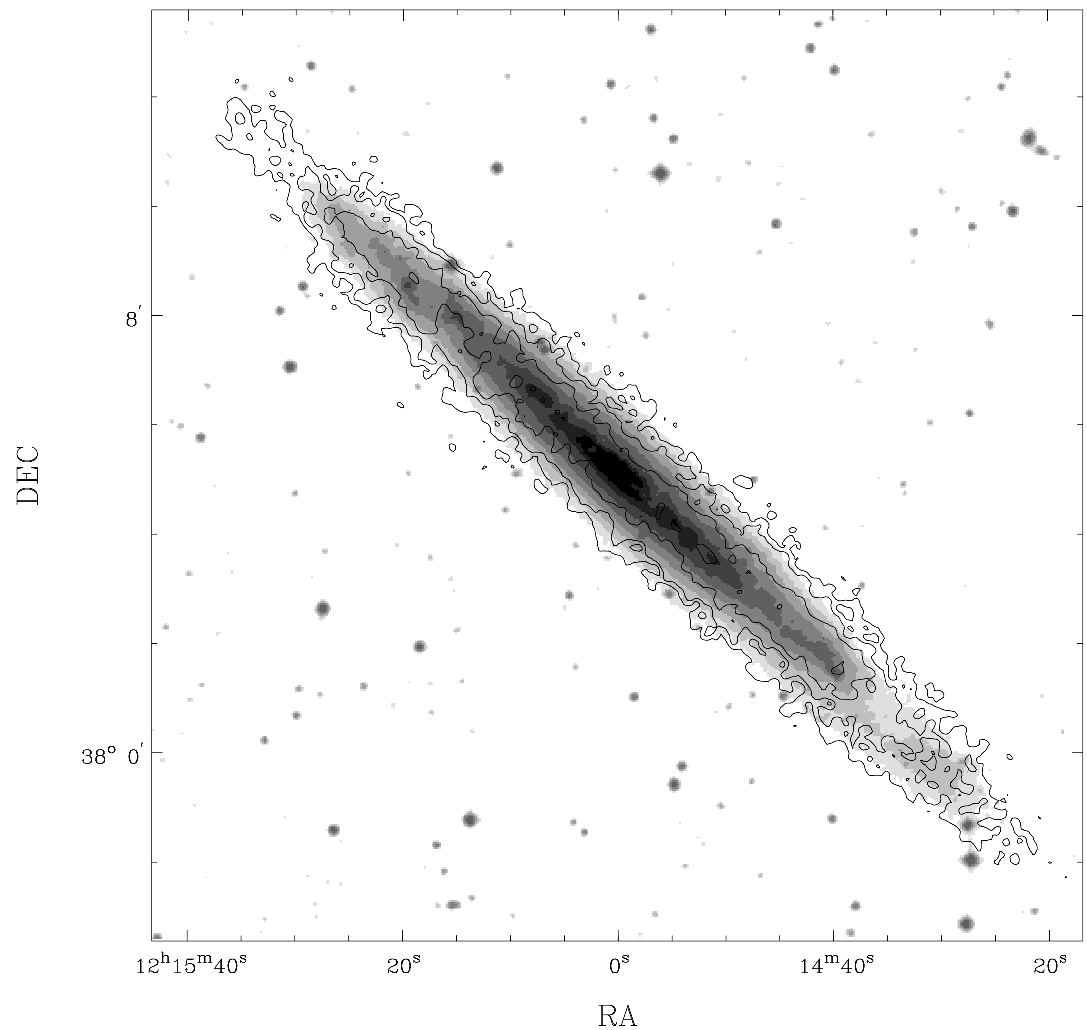

Fig. 15.— This image of NGC 4244, taken on a IIIaJ-plate, was kindly made available by Piet van der Kruit. See van der Kruit & Searle (1981a) for details. The contours ([2 4 8 16] x 6 10^{20} cm^{-2}) represent the total H I column densities at a resolution of 10″x10″ (175x175 pc). A greyscale representation of the total H I map is presented in Fig. 17.